

1 **Diet outperforms microbial transplant to drive microbiome recovery post-antibiotics**

2

3 **Co-authors:** Kennedy, M.^{1,2}, Freiburger, A.^{3,4}, Cooper, M.⁵, Beilsmith, K.³, St. George, M.L.^{5,6},

4 Kalski, M.^{5,7}, Cham, C.³, Guzzetta, A.⁸, Ng, S.C.⁹, Chan, F.K.⁹, Rubin, D.¹⁰, Henry, C.S.³,

5 Bergelson, J.^{11#}, Chang, E.B.^{5#}

6

7 ¹Medical Scientist Training Program, Pritzker School of Medicine, The University of Chicago,
8 Chicago, IL, USA

9 ²Department of Ecology & Evolution, The University of Chicago, Chicago, IL, USA

10 ³Division of Data Science and Learning, Argonne National Laboratory, Lemont, IL, United
11 States

12 ⁴Present address: Department of Chemical Engineering, Northwestern University, Evanston, IL,
13 USA

14 ⁵Department of Medicine, The University of Chicago, Chicago, IL, USA

15 ⁶Present address: University of Illinois Chicago Medical Scientist Training Program, Chicago,
16 IL, USA

17 ⁷Present address: Stritch School of Medicine, Loyola University Chicago, Chicago, IL, USA

18 ⁸Department of Pathology, The University of Chicago, Chicago, IL, USA

19 ⁹Microbiota I-Center (MagIC), Department of Medicine and Therapeutics, The Chinese
20 University of Hong Kong, Hong Kong SAR, China

21 ¹⁰Inflammatory Bowel Disease Center, University of Chicago Medicine, Chicago, IL, USA

22 ¹¹Department of Biology, Center for Genomics and Systems Biology, New York University,
23 New York, NY, USA

24

25 # co-senior authors

26

27 **ABSTRACT**

28 High-fat, low-fiber Western-style diets (WD) induce microbiome dysbiosis characterized by
29 reduced taxonomic diversity and metabolic breadth^{1,2}, which in turn increases risk for a wide
30 array of metabolic^{3–5}, immune⁶ and systemic pathologies. Recent work has established that WD
31 can impair microbiome resilience to acute perturbations like antibiotic treatment^{7,8}, although we
32 know little about the mechanism of impairment and the specific host consequences of prolonged
33 post-antibiotic dysbiosis. Here, we characterize the trajectory by which the gut microbiome
34 recovers its taxonomic and functional profile after antibiotic treatment in mice on regular chow
35 (RC) and WD, and find that only mice on RC undergo a rapid successional process of recovery.
36 Metabolic modeling indicates that RC diet promotes the development of syntrophic cross-
37 feeding interactions, while on WD, a dominant taxon monopolizes readily available resources
38 without releasing syntrophic byproducts. Intervention experiments reveal that an appropriate
39 dietary resource environment is both necessary and sufficient for rapid and robust microbiome
40 recovery, whereas microbial transplant is neither. Furthermore, prolonged post-antibiotic
41 dysbiosis in mice on WD renders them susceptible to infection by the intestinal pathogen
42 *Salmonella enterica* serovar Typhimurium. Our data challenge widespread enthusiasm for fecal
43 microbiota transplant (FMT) as a strategy to address dysbiosis and demonstrate that specific
44 dietary interventions are, at minimum, an essential prerequisite for effective FMT, and may
45 afford a safer, more natural, and less invasive alternative to FMT.

46

47

48 **INTRODUCTION**

49 An extensive body of work shows that Western-style diets (WD) with high fat and refined sugar
50 content and low dietary fiber promote gut dysbiosis characterized by reduced taxonomic
51 diversity and altered function, with significant impacts on host metabolic, immune, and other
52 organismal outcomes^{1,2}. Recent data shows that diet-induced dysbiosis predisposes the
53 microbiome to collapse after antibiotic perturbation^{7,8}, but the relative contributions of diet and
54 microbial community structure to this phenomenon are unknown, as is the extent to which the
55 resultant dynamics can be explained by metabolic interactions. Microbial dysbiosis may reduce
56 the availability of microbes to repopulate^{7,9,10}, while a poor resource environment may alter the
57 ecology of recovery and community diversification^{11,12}. Understanding these dynamics is
58 essential for choosing the most appropriate strategy for microbiome restoration. Here, we
59 compare microbiome robustness to and recovery after antibiotic perturbation across host diets,
60 and we evaluate interventions that allow us to disentangle the impacts of diet and microbial re-
61 seeding on microbiome recovery.

62

63 **RESULTS**

64 *Microbiome recovery across diets*

65 To determine how diet impacts gut microbiome resilience to antibiotic treatment, 86
66 female specific-pathogen-free (SPF) C57Bl/6 mice underwent gut microbiota homogenization¹³
67 and were then acclimated to either a standard, low-fat, high-fiber diet (regular chow, “RC”) or a
68 high-fat, low-fiber Western-style diet (“WD”) for 4 weeks. We then treated mice on each diet
69 with either a triple antibiotic cocktail (“ABX”) or 5% PBS control in the drinking water for 72
70 hours and collected fecal samples through 4 weeks (Figure 1A, Materials and Methods). To
71 assess long-term recovery, fecal samples were collected from 6 of these mice on both RC-ABX

72 and WD-ABX through 9 weeks post-ABX. One additional cohort of 12 male mice split evenly
73 across RC-ABX and WD-ABX underwent the same protocol through 2 weeks post-ABX to
74 confirm that recovery patterns were consistent across sexes (Figure S1). Given that they were,
75 we present analyses including only female cohorts unless otherwise specified.

76 We first quantified gut microbiome resilience to antibiotic treatment in terms of microbial
77 biomass by counting colony-forming units (CFUs) cultured aerobically and anaerobically on rich
78 media. We found that CFU counts dropped precipitously after antibiotic administration in both
79 treatments, but much more severely for mice on WD (Figure 1B, Table S1). Moreover, while
80 CFU counts for mice on RC had recovered to baseline levels by Day 4 post-ABX, CFU counts
81 for mice on WD did not recover to baseline through at least Day 7. Microbial biomass of PBS
82 controls remained stable in both dietary treatments (Figure S1B, Table S1).

83 We next evaluated taxonomic recovery of the gut microbiome across treatment groups
84 using 16S rRNA gene sequencing. Immediately prior to antibiotic treatment (Day -3), mice on
85 WD exhibited significantly reduced phylogenetic diversity compared to mice on RC (Figure 1C,
86 Table S2). Antibiotic-treated mice on both diets experienced a sharp decline in phylogenetic
87 diversity after antibiotic treatment. RC-ABX mice began to recover phylogenetic diversity after
88 Day 5, and recovered over half the diversity that was initially present by Day 11. For WD-ABX
89 mice, phylogenetic diversity remained severely diminished through at least Day 28 in all cohorts,
90 and up to 9 weeks post-ABX. Phylogenetic diversity in PBS controls did not change
91 significantly. Other metrics of alpha diversity (ASV richness, Shannon index) recapitulated these
92 trends (Figure S1D-F, Table S2).

93 Correspondingly, relative abundances of taxa were substantially altered during and after
94 antibiotic treatment for mice on both diets (Figure 1D). In RC-ABX mice, the microbiota passed

95 through successive stages of recolonization after antibiotic treatment, marked by early
96 dominance of facultative anaerobes like *Enterococcaceae* and *Lactobacillaceae*, followed by
97 increasing diversification of stricter anaerobes. In WD-ABX mice, the low-biomass post-ABX
98 community was dominated by *Streptococcaceae* until biomass started to recover. Recovery in
99 WD-ABX mice also passed through a successional phase of facultative anaerobes including
100 *Moraxellaceae*, *Enterococcaceae*, and *Lactobacillaceae* around Day 14, before recovering
101 stricter anaerobes. While not all specific compositional changes were precisely replicated across
102 cohorts (Figure S1G), certain characteristics, like the early dominance of facultative anaerobes as
103 biomass recovers and the post-ABX dominance of *Lactococcus* within the *Streptococcaceae*
104 family in all WD-ABX groups, were consistent.

105 PCoA of Bray-Curtis dissimilarity revealed that microbiome dynamics track a broadly
106 similar trajectory within treatment groups across all cohorts (Figure 1E, Figure S1H-I). By Day
107 14 or earlier, the gut microbiota of mice on RC-ABX approached their respective pre-ABX
108 community and corresponding RC-PBS controls, whereas the gut microbiota of WD-ABX mice
109 remained distinct from their pre-ABX community at Day 14. By Day 28, while the microbiota of
110 RC-ABX mice was indistinguishable from RC-PBS controls, only some mice on WD-ABX
111 began to approach their initial community structure (Table S2). Together, these results indicate
112 that mice on WD experience markedly impaired recovery of gut microbial taxonomic and
113 biomass recovery after antibiotic treatment compared to mice on RC.

114

115 ***Microbiome functional capacity***

116 To determine whether the gut microbiota of mice with incomplete taxonomic recovery
117 also exhibit altered functional capacity, we performed shotgun metagenomic sequencing on fecal

118 samples from a subset of mice on RC-ABX and WD-ABX at key time points before antibiotic
119 treatment and throughout recovery (Materials and Methods). Gene calls were annotated with the
120 Kyoto Encyclopedia of Genes and Genomes (KEGG) catalog for functional interpretation.

121 We first evaluated gut microbiome functional diversity by calculating functional richness
122 at different hierarchical levels (gene call, KEGG Ortholog (KO), or KEGG Category (KCat))
123 (Figure S2A). At the level of gene calls, mice on WD had reduced functional richness compared
124 to mice on RC even before antibiotic treatment (Table S3). After antibiotics, functional richness
125 of mice on both diets collapsed severely, and while mice on RC recovered up to 69% of their
126 initial gene count by Day 28, mice on WD recovered only 16%. This mirrors the taxonomic
127 trends observed in Figure 1.

128 At broader hierarchical levels like KO or KCat, functional richness was more preserved
129 during and after antibiotic treatment across both treatment groups (Figure S2A). This could
130 indicate a change in functional redundancy, i.e. the number of unique gene calls that map to each
131 KO, before and after antibiotic treatment. High functional redundancy could permit robustness at
132 the KO-level to the loss of individual gene calls. Indeed, we observe that mice on RC have
133 greater functional redundancy before antibiotics and recover significantly more functional
134 redundancy afterwards, whereas the loss of functional redundancy in mice on WD persists
135 (Figure 2A, Table S3). In mice on RC, there was a much stronger correlation between initial and
136 final functional redundancy across KOs than in mice on WD (Figure S2B, Table S3), which
137 tended to lose functional redundancy irrespective of how much redundancy a given KO began
138 with. To assess whether recovery of functional redundancy differed across functional
139 subsystems, we mapped KOs with strong (>75%) or poor (<25%) recovery of functional
140 redundancy at the KEGG system level (Figure 2B). Although there were many more KOs that

141 exhibited poor recovery in mice on WD and the majority (55%) of these mapped to metabolic
142 functions, the proportional breakdown of KEGG systems was nearly identical across treatment
143 groups and recovery levels (Figure 2B). Thus, mice on WD experience a loss in functional
144 diversity and redundancy upon antibiotic treatment that varies in intensity across KO groups,
145 with major losses in metabolic redundancy.

146 In order to focus on the most functionally interpretable aspects of our data, all subsequent
147 metagenomic analyses were performed at the KO level. We performed pairwise comparisons
148 between the pre-ABX timepoint and all post-ABX timepoints to investigate functional
149 characteristics of the microbiome throughout recovery, and to identify differentially abundant
150 KOs. Mice on RC had 658 significantly depleted KOs at Day 2 relative to pre-ABX, which grew
151 to 835 depleted KOs at Day 4, but nearly all of these recovered to baseline levels by Day 14
152 (Figure S2C). At Day 2 and Day 4, semi-overlapping but distinct subsets of genes were enriched
153 or depleted (Figure S2D-E), indicating unique intermediate functional stages during recovery.

154 Mice on WD had a larger number of significantly depleted KOs than RC counterparts at
155 all timepoints evaluated, and even by Day 28, 291 KOs had not yet returned to pre-ABX levels
156 (Figure S2F). In contrast to mice on RC, the KOs depleted at Day 14 and Day 28 were almost all
157 a subset of the KOs depleted at Day 2 (Figure S2G). Mice on WD also had small, semi-
158 overlapping sets of KOs that were significantly enriched relative to pre-ABX at all timepoints
159 (Figure S2H). Further analysis of specific functional representations across timepoints and diets
160 are presented in Figure S2I-N and Table S4).

161

162 ***WD impairs metabolome recovery***

163 To directly assay the resource environment of the gut, we performed a targeted fecal
164 metabolomic screen of gut microbiome-associated compounds including amino acids,
165 carbohydrates, bile acids (BAs), and more, from mice on RC-ABX and WD-ABX before and
166 after antibiotic treatment. As normalized metabolite abundances and dynamics were broadly
167 consistent across individual mice within dietary treatments (Figure S3A), normalized abundance
168 values were averaged across mice for visualization (Figure 2C).

169 We found that for mice on RC, the normalized abundances of many compounds were
170 distinct from baseline immediately after antibiotics, but that by Day 11, the profile returned to
171 baseline. This was statistically confirmed by PCoA clustering analysis (Figure S3B-C, Table S5).
172 Our heatmap and PCoA revealed two inflection points during recovery: the first after Day 3 and
173 the second after Day 7. The shift after Day 3 is driven largely by the dynamics of raffinose and
174 melibiose, two plant-derived α -galactoside compounds that are highly abundant in the RC diet
175 fed to our mice¹⁴. These compounds were highly elevated after antibiotics and through Day 3 but
176 returned to baseline by Day 5. The second shift reflects the dynamics of many compounds –
177 including carbohydrate monomers like ribose, glucose, and arabinose, as well as most fatty acids
178 assayed - that are depleted after antibiotics but recover between Day 7 and Day 11. The
179 secondary BAs lithocholic acid, deoxycholic acid, and 1,2-ketolithocholic acid, and to a lesser
180 extent, the primary BA cholic acid were also depleted through Day 7, but were more abundant
181 than baseline by Day 11. In stark contrast, the metabolomic profile of mice on WD showed
182 almost no signs of recovery through Day 14 (Figure 2C, Figure S3B, C). Bile acids stood out as
183 heavily depleted throughout sampling. Sucrose, niacin, and fatty acids, all of which were initially
184 depleted in mice on RC but recovered after Day 7, remained depleted throughout sampling for

185 mice on WD. Carbohydrates like cellobiose, arabinose, and myo-inositol were overly abundant
186 relative to baseline and failed to return to baseline levels.

187 Because short-chain fatty acids (SCFAs) are well documented products of microbial
188 metabolism derived from the breakdown of complex polysaccharides and can directly impact the
189 host, we performed separate metabolomic analyses to quantify absolute levels of SCFAs in cecal
190 samples from mice on RC-ABX and WD-ABX. The concentrations of acetate, butyrate, and
191 propionate at Day 14 and Day 28 in mice on RC were statistically indistinguishable from pre-
192 ABX, whereas for WD mice, they were depleted at Day 14 and persisted at low levels through
193 Day 28 (Figures 2D-F, Table S5).

194 We wondered if changes in select metabolite abundances might correspond to changes in
195 abundances of microbial genes known to produce or degrade those compounds. To assess this
196 possibility, we plotted the relative abundances of several curated subsets of microbial genes
197 across timepoints for mice on each dietary treatment and overlaid the abundances of the
198 associated metabolites (Materials and Methods). For example, melibiose and raffinose contain an
199 α -1,6 linkage that can be broken by bacterial α -galactosidase genes but not by host enzymes¹⁴. In
200 mice on RC, melibiose and raffinose reach higher concentrations after antibiotics when microbial
201 α -galactosidase genes are most depleted, and as these genes recover, melibiose and raffinose
202 abundances fall (Figure S3D, Table S6). In mice on WD, we observe few changes in the
203 abundance of α -galactosidase genes or the abundance of melibiose or raffinose. Starch and
204 arabinan can similarly be metabolized into glucose and arabinose monomers, respectively. In
205 mice on RC, both glucose and arabinose reach low abundance when genes for starch and
206 arabinose metabolism drop, and as those polysaccharide metabolism genes rise in abundance, so
207 does the abundance of the respective monomeric breakdown product (Figure S3E, F). In mice on

208 WD, there are again few changes in either metabolite or gene abundances over the course of
209 recovery. These data suggest that in mice on RC diet, the microbiota may respond to or interact
210 with the resource environment, and especially with complex carbohydrates like those analyzed
211 here, in a way that the microbiota of mice on WD does not.

212

213 ***Metabolic modeling of recovery dynamics***

214 Across all taxonomic and functional metrics evaluated, mice on WD experienced more
215 severe ecosystem collapse with slower and less complete recovery than mice on RC (Figures 1-
216 2). This was not attributable to slower antibiotic clearance in mice on WD (Figure S4, Table S7).
217 To explore the mechanism by which resource environment shapes our observed community
218 recovery patterns, we developed metabolic models that leverage functional knowledge of
219 microbiome members and integrated ‘omics data to predict the metabolic interactions and
220 dynamics of each community over time (Materials and Methods). Most of the ASVs presented in
221 Figure 1 closely match 16S sequences found in at least one fully annotated isolate genome in
222 RefSeq, which we used to reconstruct representative probabilistic genome-scale metabolic
223 models (prGEMs) through the ModelSEED2 pipeline in KBase. We simulated these ASV-based
224 prGEMs to calculate the probability that each strain can take up, grow on, or excrete the
225 compounds in our metabolomics assay, producing strain-metabolite interaction probability
226 profiles (SMIPPs). Clustered heatmaps of these SMIPPs (Figure S5) suggest metabolic
227 specialization among certain ASVs, and create a roadmap for understanding how each ASV can
228 metabolically interact with others in the community.

229 We then combined the SMIPPs with our 16S-based ASV-abundance profiles to compute
230 microbiome-metabolite interaction probability profiles (MMIPPs) for each sample. These

231 MMIPPs predict sample-wide metabolite consumption, conversion, and production capacity by
232 component ASVs. Correlations of MMIPPs with measured metabolite abundances (Table S8)
233 reveal that melibiose and cellobiose have higher correlations with predicted microbial
234 consumption and production: these metabolites are abundant in samples predicted to produce the
235 compounds, and scarce in samples predicted to consume them. This suggests interdependence
236 between the dynamics of these compounds and microbiome metabolism.

237 To better understand which metabolic functions were performed by which ASVs over the
238 course of recovery and how this differed across diets, we next combined our ASV-based
239 prGEMs into community models and, for each interval between timepoints, simulated the flux
240 through each metabolic pathway within the constraints of our observed metabolite and ASV
241 abundance dynamics. These simulations determined the most likely metabolic behavior of the
242 ASVs in each interval (Figure 3A, Table S8), and revealed profound metabolic differences
243 between the RC and WD treatment groups. In the RC communities, ecological complexity and
244 syntrophic cross-feeding interactions are maintained in the immediate aftermath of antibiotic
245 treatment and throughout recovery (Figure 3B, Figure S6). By contrast, in WD communities,
246 almost all syntrophic interactions are lost in the aftermath of antibiotic treatment through Day 7-
247 11. Instead, the WD communities are dominated by a single Lactococcus ASV with broad
248 metabolic capacity that produces few syntrophic byproducts. The RC community contains this
249 same Lactococcus ASV, but in the RC dietary context, it is balanced by trophic complexity and
250 interdependencies with other strains, and never dominates the microbiome. Although amino
251 acids are excluded from Figure 3A for visual clarity, the observed patterns of greater metabolic
252 interactivity, syntropy, and complexity in the RC microbiome compared to WD apply to amino
253 acid metabolism as well (Figure 3B, Table S8).

254 The community simulations further reveal a pattern of metabolic succession in the
255 recovery of the RC microbiome. Muribaculum abundance declines following antibiotic
256 treatment, leaving open a niche for the consumption of cellobiose. This is filled by various
257 Enterococci, which consume cellobiose and raffinose and produce metabolic products like citrate
258 and malate, and thereby cultivate a niche for Acinetobacter to emerge. The continued production
259 of malate from Enterococcus and the production of myristate from Acinetobacter open a niche
260 for Akkermansia, and the complex carbohydrate consumers Alistipes and Muribaculum. By Day
261 7-11, Muribaculum has largely replaced Enterococcus as the primary consumer of cellobiose and
262 raffinose, as in the pre-antibiotic state. The partial recovery observed in WD mice between Day 7
263 -14 also seems to be mediated by the emergence of Enterococcus. In this dietary context
264 however, they are insufficient to shift the community towards complete recovery.

265 Collectively, our model suggests that metabolism of complex carbohydrates like
266 cellobiose and raffinose, which are relatively more abundant in RC than in the purified WD,
267 drive the syntrophic interactions that facilitate succession, diversification, and recovery. On WD,
268 despite the microbiome's overlapping taxa and relatively broad capacity to metabolize the same
269 compounds after antibiotics, the greater availability of simple sugars promotes dominance of a
270 single taxon. Thus, dietary resource availability fundamentally shapes the way that available taxa
271 interact with their environment and other microbes to promote or prevent recovery.

272

273 ***Dietary intervention versus FMT***

274 Our data suggest that recovery in WD is limited primarily by an imbalance in the
275 availability of simple and complex carbohydrates across dietary treatments rather than lack of
276 metabolically capable taxa. To test this, we performed intervention experiments in which diet

277 and microbial re-exposures were controlled after antibiotic treatment (Figure 4A, Materials and
278 Methods). Briefly, after antibiotic treatment, mice on each pre-antibiotic diet were transferred
279 into sterile gnotobiotic cages, and different post-antibiotic diet (“ RC_D ”, “ WD_D ”) and/or microbial
280 re-exposures (“ RC_M ”, “ WD_M ”) were administered in a factorial manner: for mice on each pre-
281 antibiotic diet, we changed either microbial re-exposure, diet, both, or neither. Microbial re-
282 exposure was administered via FMT at 24 hours post-antibiotics and again at Day 14; one group
283 on each diet received sterile PBS_M gavage as a no-transplant control. Fecal samples were
284 collected before and after antibiotic treatment, and weekly through Day 28 of recovery. We
285 selected Day 14 as the most salient timepoint to evaluate the distinct recovery dynamics of mice
286 on RC and WD (full time course data available in Figure S7, Supplementary Discussion). No-
287 ABX controls on each diet serve as benchmarks for “recovery,” which was evaluated in terms of
288 overall community composition via 16S rRNA sequencing (Figure 4B) and further quantified by
289 PCoA clustering analysis (Figure S7, Table S9) and ASV richness (Figure 4C).

290 We first confirmed that this experimental model recapitulates the phenotypes of our
291 original experiments: mice that did not change dietary or microbial re-exposures ($RC \rightarrow$
292 RC_D/RC_M and $WD \rightarrow WD_D/WD_M$) matched the RC -ABX and WD -ABX phenotypes described
293 in Figure 1 (i.e. RC recovered gut microbiota composition and alpha diversity, WD did not).
294 From relative abundance plots, we see that irrespective of pre-ABX diet or post-ABX microbial
295 transplant, gut microbiota composition broadly segregates on the basis of post-ABX diet (Figure
296 4B). PCoA analysis statistically confirms that gut microbial composition segregates across PC1
297 by post-ABX diet, with mice on RC_D uniformly falling lower on PC1 and closer to the no-ABX
298 controls than mice on WD_D (Figure S7, Table S9). Similarly, mice on post-ABX RC_D uniformly
299 recovered more ASV richness by D14 than all WD_D counterparts (Figure 4C, Table S9).

300 Among mice that were fed post-ABX WD_D, microbial transplant had negligible impact
301 on recovery, with all WD_D treatment groups exhibiting severely diminished ASV richness and
302 clustering distinctly from WD no-ABX controls at D14. These experiments indicate that an
303 appropriate diet is both necessary and sufficient for rapid and robust gut microbiota recovery
304 after antibiotic treatment, while microbial transplant is neither. This broadly supports our
305 modeling predictions that recovery is predominantly driven by dietary resource availability
306 (especially the balance of simple and complex carbohydrates) rather than by the presence or
307 absence of specific taxa.

308

309 ***Prolonged loss of colonization resistance***

310 Under healthy conditions, the microbiome protects the host via “colonization resistance”
311 against opportunistic pathogens¹⁵. For example, the pathogen *Salmonella enterica* serovar
312 *Typhimurium* (*St*) is unable to establish lower GI infection or cause colitis in SPF mice unless
313 they have been pre-treated with streptomycin¹⁶. While established models of *St* colonization
314 resistance require pre-treatment with antibiotics for 24 hours immediately before *St* challenge,
315 we wondered if the prolonged post-antibiotic dysbiosis experienced by mice on WD might
316 render them more susceptible to opportunistic infection by *St* as late as 14 days after antibiotic
317 treatment has ended.

318 To evaluate this possibility, we performed a series of experiments including 5 cohorts of
319 female mice and one cohort of male mice in standard, non-gnotobiotic cages (Materials and
320 Methods). After antibiotic or PBS administration, mice recovered for 14 days, as in other
321 experiments, and then each dietary and antibiotic treatment group was split into infection and no-
322 infection treatment groups (Figure 5A). WD has been shown to facilitate *St* infection relative to

323 RC even without antibiotic pre-treatment¹⁷; by comparing ABX and no-ABX control groups on
324 each diet, we can isolate the specific effects of diet versus diet-induced post-antibiotic dysbiosis.
325 Fecal samples and body weights were collected at t=6, 12, 24, 48, 72, and 96 hours post-
326 infection (hpi). As trends were consistent across male and female cohorts (Figure S8), data were
327 combined to improve statistical power.

328 We first evaluated *St* load at each timepoint after infection (Figure 5B). Uninfected
329 controls had undetectable levels of *St*, confirming no contamination. As hypothesized, mice on
330 WD-ABX-INF were the most susceptible to infection, exhibiting significantly higher *St* loads
331 than all other treatment groups from t=24-48 hpi and reaching ~10⁵-fold higher median infection
332 load than the WD-PBS-INF group during this period (Table S10). From 72-96 hpi, both the WD-
333 ABX-INF and WD-PBS-INF groups had significantly greater infection load than all groups on
334 RC diet, recapitulating previous findings that WD alone is sufficient to impair colonization
335 resistance. Although the WD-ABX-INF group had greater median *St* load than WD-PBS-INF
336 through 96 hpi, this difference was no longer significantly different after 48 hpi.

337 We performed targeted analyses of infection severity in lower GI tissues to focus on the
338 enteric colonization resistance (rather than disseminated typhoid) model of *St* infection (gross
339 body weight data are available in Figure S8, Supplementary Discussion)^{16,18}. Histopathological
340 scoring and qPCR analysis of a panel of *St*-induced inflammatory markers in cecal tissue
341 revealed that the WD-ABX-INF group experienced significantly more severe inflammatory
342 pathology (mean histopathology score = 10.21 ± 2.126, Figures 5C, D, Figure S8, Table S10)
343 with higher expression of inflammatory markers (Figures 5E-G, Figure S8, Table S10) than all
344 other treatment groups. Interestingly, the uninfected WD-ABX-PBS control group experienced
345 variable but occasionally severe inflammation (mean histopathology score = 6.5 ± 4.65)

346 comparable to the WD-ABX-INF group, suggesting that antibiotic treatment in mice on WD can
347 induce inflammation even without *St* challenge. Together, these results indicate that only the
348 WD-ABX-INF group consistently succumbed to lower-GI infection and enteritis, supporting the
349 hypothesis that prolonged post-antibiotic dysbiosis in mice on WD impairs colonization
350 resistance in the lower GI tract relative to mice that were not pre-treated with antibiotics, or that
351 were on RC diet.

352

353 **DISCUSSION**

354 Our experiments reveal that WD and antibiotic treatment collectively cause more severe
355 and prolonged microbial ecosystem collapse than observed for either factor alone. This collapse
356 entails extreme loss of taxonomic diversity, as previously reported^{7,8}, as well as reduced
357 functional redundancy and a skewed metabolome. Metabolic modeling indicates that recovery in
358 mice on RC is driven by the development of syntrophy as complex carbohydrates are
359 metabolized and simpler byproducts open niche space in the community. Although the
360 microbiota of mice on WD retains the metagenomic capacity to perform these same reactions
361 after antibiotic treatment, the easy availability of simple dietary sugars promotes dominance by a
362 single metabolic generalist and prevents progression along the same successional trajectory.
363 These findings are supported by our intervention experiments, in which we showed that without
364 an appropriate dietary resource environment, microbial communities will fail to recover,
365 irrespective of microbial transplant. Last, we show that prolonged post-antibiotic dysbiosis in
366 mice on WD can extend the window of susceptibility to opportunistic pathogens like *St*.

367 Given that our WD formulation is designed to reflect typical American consumption
368 patterns¹⁹ and that antibiotics are liberally prescribed for an enormous array of pathologies^{20,21},

369 these findings bear great clinical relevance. In humans, variability in microbiome recovery after
370 antibiotics is well documented, but poorly understood^{22–26}. Our data suggest that diet may play a
371 central role in driving inter-individual differences in microbiome recovery and should be
372 explicitly assessed in human studies. Moreover, we must consider the risks of prolonged and
373 severe post-antibiotic dysbiosis for populations vulnerable to opportunistic infection, like
374 immunocompromised individuals, or those experiencing chronic disease. For instance, severe
375 cases of ulcerative colitis are often treated with antibiotics²⁷. Individuals with ulcerative colitis
376 also often maintain restrictive diets to prevent flares²⁸. The combination of limited diet and
377 antibiotic treatment may paradoxically predispose these individuals to exacerbated microbiome
378 dysbiosis, which may feed back into the cycle of disease. Appropriate peri-antibiotic dietary
379 interventions should be investigated across clinical contexts as a safe and affordable route to
380 promote microbiome recovery when antibiotics must be used.

381 To date, the growing field of microbiome therapeutics has centered largely around
382 microbial replacement strategies like fecal microbiota transplant (FMT)²⁹, probiotics³⁰, or live
383 biotherapeutics³¹, which have shown widely variable efficacy across individuals and diseases.
384 Our intervention experiments indicate that diet is more foundational to recovery than microbial
385 re-seeding, and that without an appropriate dietary resource environment, microbial transplant is
386 insufficient to promote recovery. Even under controlled lab conditions using autologous FMT of
387 a mature, diverse community in genetically matched, diet-controlled recipients, the outcomes of
388 microbial transplant were variable and ultimately dependent upon post-antibiotic diet. In contexts
389 with more significant microbial extinction than in our experiments, microbial replacement may
390 yet play an important role in recovery, as has been extensively shown^{7,9,10}. However, our data
391 suggest that unless the microbial transplant encounters an environment with the right resources

392 to support engraftment, growth, and diversification in the recipient, its efficacy will be limited at
393 best. Thus, concomitant dietary interventions may improve the consistency and efficacy of
394 existing microbial transplant strategies.

395 Finally, we propose ecological succession as a novel paradigm for approaching
396 microbiome restoration. Under this model, both the taxa present and their surrounding resource
397 environment interact in an iterative feedback process to guide the progression of the community
398 from one stage to the next^{32,33}. Early arriving microbes may facilitate or inhibit the growth of
399 later arriving microbes by producing metabolic byproducts for cross-feeding³⁴ or by changing the
400 resource environment (e.g. oxygen levels³⁵, pH³⁶, bile acid pool³⁷). The community cannot
401 proceed to the next stage if it is either missing the right taxa, or if the taxa do not have access to
402 the right resources. Our data and simulations indicate that WD does not provide the right balance
403 of simple and complex carbohydrates to initiate this successional process even when the right
404 taxa are present. In this sense, FMT in mice on WD is akin to transplanting a mature forest into
405 barren soil after a fire: the soil is unable to accommodate its growth. By using approaches like
406 the metabolic model presented here, we can resolve the transitional dynamics between healthy
407 and disease states and learn to support succession at each stage by matching specific dietary or
408 microbial interventions to the present needs of the community. In this way, we can promote the
409 environmental change necessary for the ecosystem to once again accommodate the growth of the
410 climax community.

411

412 REFERENCES

- 413 1. Bisanz, J. E., Upadhyay, V., Turnbaugh, J. A., Ly, K. & Turnbaugh, P. J. Meta-Analysis Reveals
414 Reproducible Gut Microbiome Alterations in Response to a High-Fat Diet. *Cell Host & Microbe* **26**,
415 265-272.e4 (2019).

- 416 2. Sonnenburg, E. D. & Sonnenburg, J. L. Starving our Microbial Self: The deleterious consequences
417 of a diet deficient in microbiota-accessible carbohydrates. *Cell Metabolism* **20**, 779–786 (2014).
- 418 3. Nieuwdorp, M., Gilijamse, P. W., Pai, N. & Kaplan, L. M. Role of the Microbiome in Energy
419 Regulation and Metabolism. *Gastroenterology* **146**, 1525–1533 (2014).
- 420 4. Asnicar, F. *et al.* Microbiome connections with host metabolism and habitual diet from 1,098 deeply
421 phenotyped individuals. *Nat Med* **27**, 321–332 (2021).
- 422 5. Turnbaugh, P. J. *et al.* An obesity-associated gut microbiome with increased capacity for energy
423 harvest. *Nature* **444**, 1027–131 (2006).
- 424 6. Levy, M., Kolodziejczyk, A. A., Thaiss, C. A. & Elinav, E. Dysbiosis and the immune system.
425 *Nature Reviews Immunology* **2017** *17*, 219–232 (2017).
- 426 7. Ng, K. M. *et al.* Recovery of the Gut Microbiota after Antibiotics Depends on Host Diet, Community
427 Context, and Environmental Reservoirs. *Cell Host and Microbe* **26**, 650–665.e4 (2019).
- 428 8. Tanes, C. *et al.* Role of dietary fiber in the recovery of the human gut microbiome and its
429 metabolome. *Cell Host & Microbe* **29**, 394–407.e5 (2021).
- 430 9. Taur, Y. *et al.* Reconstitution of the gut microbiota of antibiotic-treated patients by autologous fecal
431 microbiota transplant. *Sci Transl Med* **10**, eaap9489 (2018).
- 432 10. Tropini, C. *et al.* Transient Osmotic Perturbation Causes Long-Term Alteration to the Gut
433 Microbiota. *Cell* **173**, 1742–1754.e17 (2018).
- 434 11. Shade, A. *et al.* Fundamentals of Microbial Community Resistance and Resilience. *Frontiers in
435 Microbiology* **3**, (2012).
- 436 12. May, R. M. Will a Large Complex System be Stable? *Nature* **238**, 413–414 (1972).
- 437 13. Miyoshi, J. *et al.* Minimizing confounders and increasing data quality in murine models for studies of
438 the gut microbiome. *PeerJ* **6**, e5166 (2018).
- 439 14. Kennedy, M. S. *et al.* Dynamic genetic adaptation of *Bacteroides thetaiotaomicron* during murine gut
440 colonization. *Cell Rep* **42**, 113009 (2023).

- 441 15. Buffie, C. G. & Pamer, E. G. Microbiota-mediated colonization resistance against intestinal
442 pathogens. *Nature Reviews Immunology* **13**, 790–801 (2013).
- 443 16. Barthel, M. *et al.* Pretreatment of Mice with Streptomycin Provides a *Salmonella enterica* Serovar
444 Typhimurium Colitis Model That Allows Analysis of Both Pathogen and Host. *Infection and*
445 *Immunity* **71**, 2839 (2003).
- 446 17. Wotzka, S. Y. *et al.* *Escherichia coli* limits *Salmonella Typhimurium* infections after diet shifts and
447 fat-mediated microbiota perturbation in mice. *Nat Microbiol* **4**, 2164–2174 (2019).
- 448 18. Santos, R. L. *et al.* Animal models of *Salmonella* infections: enteritis versus typhoid fever. *Microbes*
449 and *Infection* **3**, 1335–1344 (2001).
- 450 19. NHANES. *NHANES - What We Eat in America: Nutrient Intakes from Food by Gender and Age*. vol.
451 National Health and Nutrition Examination Survey Data. (U.S. Department of Health and Human
452 Services, Centers for Disease Control and Prevention, Hyattsville, MD, 2009).
- 453 20. Wang, J., Wang, P., Wang, X., Zheng, Y. & Xiao, Y. Use and Prescription of Antibiotics in Primary
454 Health Care Settings in China. *JAMA Internal Medicine* **174**, 1914–1920 (2014).
- 455 21. Bell, M. Antibiotic Misuse: A Global Crisis. *JAMA Internal Medicine* **174**, 1920–1921 (2014).
- 456 22. Dethlefsen, L. & Relman, D. A. Incomplete recovery and individualized responses of the human
457 distal gut microbiota to repeated antibiotic perturbation. *Proceedings of the National Academy of*
458 *Sciences of the United States of America* **108**, 4554–4561 (2011).
- 459 23. Shaw, L. P. *et al.* Modelling microbiome recovery after antibiotics using a stability landscape
460 framework. *The ISME Journal* **13**, 1845–1856 (2019).
- 461 24. Zaura, E. *et al.* Same Exposure but two radically different responses to antibiotics: Resilience of the
462 salivary microbiome versus long-term microbial shifts in feces. *mBio* **6**, (2015).
- 463 25. Palleja, A. *et al.* Recovery of gut microbiota of healthy adults following antibiotic exposure. *Nature*
464 *Microbiology* **3**, 1255–1265 (2018).
- 465 26. Chng, K. R. *et al.* Metagenome-wide association analysis identifies microbial determinants of post-
466 antibiotic ecological recovery in the gut. *Nature Ecology and Evolution* **4**, 1256–1267 (2020).

- 467 27. Ledder, O. & Turner, D. Antibiotics in IBD: Still a Role in the Biological Era? *Inflammatory Bowel
468 Diseases* **24**, 1676–1688 (2018).
- 469 28. Jowett, S. L. *et al.* Influence of dietary factors on the clinical course of ulcerative colitis: a
470 prospective cohort study. *Gut* **53**, 1479–1484 (2004).
- 471 29. Cohen, N. A. & Maharshak, N. Novel Indications for Fecal Microbial Transplantation: Update and
472 Review of the Literature. *Dig Dis Sci* **62**, 1131–1145 (2017).
- 473 30. Ritchie, M. L. & Romanuk, T. N. A Meta-Analysis of Probiotic Efficacy for Gastrointestinal
474 Diseases. *PLoS ONE* **7**, e34938 (2012).
- 475 31. O'Toole, P. W., Marchesi, J. R. & Hill, C. Next-generation probiotics: the spectrum from probiotics
476 to live biotherapeutics. *Nat Microbiol* **2**, 1–6 (2017).
- 477 32. Gilbert, J. A. & Lynch, S. V. Community ecology as a framework for human microbiome research.
478 *Nat Med* **25**, 884–889 (2019).
- 479 33. Prach, K. & Walker, L. R. Four opportunities for studies of ecological succession. *Trends in Ecology
480 & Evolution* **26**, 119–123 (2011).
- 481 34. Douglas, A. E. The microbial exometabolome: ecological resource and architect of microbial
482 communities. *Philosophical Transactions of the Royal Society B: Biological Sciences* **375**, 20190250
483 (2020).
- 484 35. Lee, J.-Y., Tsolis, R. M. & Bäumler, A. J. The microbiome and gut homeostasis. *Science* **377**,
485 eabp9960 (2022).
- 486 36. Van Herreweghen, F., De Paepe, K., Roume, H., Kerckhof, F.-M. & Van de Wiele, T. Mucin
487 degradation niche as a driver of microbiome composition and Akkermansia muciniphila abundance in
488 a dynamic gut model is donor independent. *FEMS Microbiology Ecology* **94**, fiy186 (2018).
- 489 37. Ridlon, J. M., Kang, D. J., Hylemon, P. B. & Bajaj, J. S. Bile acids and the gut microbiome. *Current
490 Opinion in Gastroenterology* **30**, 332–338 (2014).
- 491

492 **FIGURE LEGENDS**

493 **Figure 1: Bacterial biomass and taxonomic recovery after antibiotic treatment are**
494 **impaired in mice on WD.** (A) Mice on RC or WD were treated with PBS or ABX in the
495 drinking water for 72 hours, and serial fecal samples were collected to assess microbiome
496 recovery (Materials and Methods). (B) Fecal microbial biomass in mice on RC-ABX and WD-
497 ABX for mice from Cohort 1 (n=6/group). Error bars indicate mean \pm SD. Statistics including
498 exact *n* and *P* values are presented in Tables S1. See also Figure S1B, S1C. (C) Fecal alpha
499 diversity (phylogenetic diversity) of mice across dietary treatments and timepoints (all cohorts,
500 n=4-13/group). Error bars indicate mean \pm SD. Statistics including exact *n* and *P* values are
501 presented in Tables S2. (D) Mean relative abundances of different microbial families for Cohort
502 1 (n=6 mice/group, See Fig. S1G for other cohorts). (E) PCoA of 16S-based microbiome
503 taxonomic composition at the genus level using Bray-Curtis dissimilarity for samples from all
504 treatment groups and cohorts through Day 14. See Fig. S1H for results through Day 28.

505

506 **Figure 2: Functional recovery is severely impaired in mice on WD.** (A) Functional
507 redundancy (mean genes per KO) of mice on RC-ABX and WD-ABX (n=2-8/group). Error bars
508 indicate mean \pm SD. Statistics including exact *n* and *P* statistics are presented in Table S3. (B)
509 KEGG system mapping of KOs that recovered < 25% or > 75% of their pre-ABX Day -3
510 functional redundancy across RC-ABX and WD-ABX groups. (C) Heatmap displaying
511 log2FoldChange in metabolite abundances relative to the pre-ABX Day -3 timepoint, averaged
512 across n=3-6 mice/group. (D – F) Absolute concentrations of (D) acetate, (E) butyrate, (F)
513 propionate in mice on RC-ABX (blue) and WD-ABX (red) (n=3-4/group, **q* < 0.05, ***q* < 0.01).

514 Whiskers represent median $\pm 1.5^{\circ}\text{IQR}$. Statistics including exact n and P values are presented in
515 Table S5.

516

517 **Figure 3: Metabolic modeling predicts poor syntrophy in mice on WD.** (A) Community flux
518 simulations over each time interval for mice on RC-ABX or WD-ABX. Edges represent
519 predicted flux (dashed = consumption, solid = production) and nodes represent metabolites
520 (orange) or ASV prGEMs (red). Select fluxes predicted to play a crucial role in recovery are
521 highlighted in green and purple; other fluxes are grey. Map includes all measured metabolites
522 with fluxes > 0.05 excluding niacin, acetate, propionate, and amino acids for visual clarity, but
523 full model with all flux values is available in Table S8. Interactive map with flux values is
524 available at https://modelseed.org/annotation/projects/gut_microbiome/. (B) Number of
525 syntrophic interactions identified in the community models for mice on RC (blue) and WD (red)
526 by category over each time interval.

527

528 **Figure 4: Dietary intervention facilitates microbiome recovery from antibiotics.** (A)
529 Experimental design. After ABX or PBS, post-ABX dietary treatments (RC_D , WD_D) were
530 provided ad libitum from day 0 through the end of the experiment; post-ABX microbial
531 treatments (RC_M , WD_M , PBS_M) were administered at Day 1 and Day 14. (B) Mean relative
532 abundances of microbial families at Day 14 across treatment groups ($n=5-8$ mice/group). (C)
533 ASV richness across treatment groups at Day 14 ($n=5-8$ /group). Whiskers indicate median \pm
534 1.5°IQR . Statistics including exact n and P values are presented in Table S9.

535

536 **Figure 5: Prolonged post-antibiotic dysbiosis in mice on WD impairs colonization**

537 **resistance to St.** (A) Experimental treatment groups. (B) Fecal St load (CFU/g) among infected
538 treatment groups. Uninfected controls had no detectable *St* and are not depicted. Error bars
539 indicate median \pm 1.5*IQR. Statistics including exact *n* and *P* values are presented in Table S10.
540 (C) Representative histological images of mice in different treatment groups. (D)
541 Histopathological scoring of cecal sections from mice on indicated treatment groups at 96 hpi
542 (*n*=5–13/group, Figure S8). Error bars indicate mean \pm SD. Statistics including exact *n* and *P*
543 values are presented in Table S10. (E – G) mRNA expression of immune genes in cecal mucosal
544 scrapings at *t*=96 hpi based on RT-qPCR (see Figure S8 for additional inflammatory markers).
545 Expression is normalized to the housekeeping gene Actb and the RC-PBS-PBS treatment group
546 (*n*=3-13/group). Whiskers indicate median \pm 1.5*IQR. Statistics including exact *n* and *P* values
547 are presented in Table S10.

548

549 MATERIALS AND METHODS

550 *Mice*

551 C57Bl/6 mice at 5 weeks of age were purchased from The Jackson Laboratory barrier facility
552 EM04 and co-housed in cages of 2-4 mice with pine shavings bedding in standard barrier
553 facilities unless otherwise specified. All mice underwent a two-step microbiome homogenization
554 protocol: 1) bedding was mixed across all cages twice a week from age 5-8 weeks leading up to
555 the beginning of each experiment to reduce intra-cohort cage effects, and 2) mice were gavaged
556 once at 6-weeks with fecal material banked from our SPF colony to reduce inter-cohort
557 differences in microbiome composition¹³. Mice were fed autoclaved standard RC diet (LabDiets
558 5K67) during microbiome homogenization. Most experiments used only female mice to
559 minimize variability introduced by sex, but one male cohort was included to ensure that

560 phenotypes were consistent across sexes. This cohort was formally part of the colonization
561 resistance experiment, which underwent an identical protocol to all other experiments through
562 Day 14 of recovery. All mouse experiments were conducted in accordance with the University of
563 Chicago Institutional Biosafety Committee and Institutional Animal Care and Use Committee.

564

565 ***Diet Acclimation and Antibiotic Treatment***

566 Mice at 8 weeks of age were either maintained on RC diet (LabDiets 5K67) or switched to WD
567 (Envigo TD.97222)³⁸ to acclimate for 4 weeks. This diet was designed to broadly reflect the
568 nutritional intake of a Western population based on the Center for Disease Control and
569 Prevention's National Health and Nutrition Examination Survey¹⁹. During diet acclimation,
570 bedding was mixed across cages within diet treatments twice a week. At 12 weeks of age, mice
571 on each diet were treated with a sterile-filtered triple antibiotic cocktail of vancomycin (0.5
572 mg/ml), neomycin (1.0 mg/ml), and cefoperazone (0.5mg/ml) or 5% sterile PBS control in the
573 drinking water for 72 hours. Water consumption was monitored during this time to ensure
574 adequate treatment (Figure S1A).

575

576 ***Western Diet Microbiome Resilience Experiments***

577 Three female cohorts of mice were used in these experiments (including the long-term cohort
578 described below). After treatment with antibiotics or PBS control, mice were maintained on their
579 respective pre-antibiotic diets, and fecal samples were collected for 4 weeks after cessation of
580 antibiotics on days -31, -3, 0, 1-8, 11, 14, 16, 18, 21, 23, 25, and 28. Cages were changed on days
581 -38, -24, -10, 7, and 21. Subsets of mice were sacrificed at the pre-antibiotic (Day -3), post-

582 antibiotic (Day 0), week two of recovery (Day 14), or week four of recovery (Day 28) timepoints
583 (total n=4/timepoint/treatment group).

584

585 ***Western Diet Microbiome Resilience – Long-term Recovery Cohort***

586 One cohort of 8-week old female C57Bl/6 mice (n=6/group, RC-ABX and WD-ABX only) was
587 bred in our animal facility for this experiment. Mice were co-housed in cages of 3 mice with pine
588 shavings bedding in standard barrier facilities and did not undergo the microbiome
589 homogenization protocol. These mice were acclimated to their respective dietary treatment for
590 only 10 days. Although 10-days of diet acclimation was predicted to be sufficient for
591 microbiome stabilization, which can occur within 4 days³⁹, we lengthened the diet acclimation
592 phase in subsequent cohorts to ensure that host physiological differences across dietary groups
593 had stabilized⁴⁰. During diet acclimation, bedding was mixed across cages within diet treatments
594 twice a week. Antibiotic treatment was administered as described above. Fecal samples were
595 collected for 9 weeks after cessation of antibiotics on days -31, -3, 0, 0.5, 1, 1.5, 2-8, 11, 14, 16,
596 18, 21, 28, 35, 49, and 63, and then all mice were sacrificed. Cage changes were performed on
597 days -10, 7, 21, 35, and 49. Experimental duration was decreased after this cohort as microbiome
598 recovery appeared to stabilize by Day 28 (Fig. S1).

599

600 ***Post-antibiotic Intervention Experiments***

601 Four cohorts of female mice were used in these experiments (n=8/treatment group, n=96 total).
602 For each cohort, 24 mice at 5 weeks of age were split across 4 cages (n=6/cage) in standard
603 barrier facilities for 3 weeks of microbiome homogenization. After microbiome homogenization,
604 mice were transferred into 8 hermetically sealed gnotobiotic Techniplast IsoCage P Bioexclusion

605 cages for diet acclimation and antibiotic treatment as described above (n=3/cage). Immediately
606 following antibiotic treatment (Day 0), mice were transferred into 12 new sterile gnotobiotic
607 cages and post-antibiotic diet and microbial re-exposure treatments were administered
608 (n=2/treatment group/cohort). For microbial re-exposure treatments, fecal material was collected
609 from all mice on the day before antibiotic treatment (Day -1), pooled by dietary treatment,
610 resuspended at 60 mg/ml in 25% glycerol solution, and frozen at -80°C until administration.
611 Microbial re-exposures were administered by oral gavage of 200 µl of the respective fecal
612 solution or sterile PBS at 24 hours after cessation of antibiotics (Day 1) and were re-administered
613 at Day 14 of recovery after cage changes were performed to ensure that dispersal limitation did
614 not impair microbiome recovery. Fecal samples were collected on days -31, -3, 0, 7, 14, 21, and
615 28, and mice were sacrificed at Day 28 post-antibiotics.

616 All procedures on the IsoCage P rack system from the time of antibiotic administration
617 onward were performed using a modified sterile technique necessitated by the logistics of
618 handling such a large number of treatment groups: one researcher donned sterile garb including
619 two pairs of sterile gloves, the workspace was covered with a sterile drape, and another team
620 member assisted in manipulation of the outside of the cages. The sterile team member performed
621 all mouse manipulations without making contact with anything outside of the cage or sterile
622 field. In between treatment groups, the sterile team member donned new sterile gloves, but
623 otherwise continued to use the same garb.

624

625 ***Colonization Resistance Experiments***

626 After diet acclimation and antibiotic or PBS administration, 4 cohorts of female mice (n=3-
627 6/treatment group) and one cohort of male mice (n=6/treatment group, RC-ABX-INF and WD-

628 ABX-INF only) were allowed to recover for 14 days, and were then inoculated by oral gavage
629 with 200 µl of either nalidixic acid-resistant *Salmonella enterica* serovar Typhimurium (*St*, strain
630 IR715)⁴¹ or PBS control. To prepare the gavage solution, *St* was grown aerobically in Luria
631 Broth (LB) media at 30°C with shaking at 250RPM for 14 hours. Cultures were pelleted by
632 centrifuging for 5 minutes at 4000xg and resuspended at 1:100 dilution in PBS (final infection
633 dose: ~7 x 10⁷ CFU/mouse). Fecal samples and body weights were collected for 4 days post-
634 infection, and then mice were sacrificed.

635

636 ***Tissue Harvest and Sample Processing***

637 All mice were euthanized by CO₂ asphyxiation and death was confirmed via cervical dislocation.
638 After sacrifice, blood was collected by cardiac puncture and serum was isolated and stored at -
639 80°C. Liver, spleen, mesenteric lymph nodes, and mesenteric, gonadal, inguinal, and
640 retroperitoneal fat deposits were weighed and split across samples that were preserved for
641 histology, snap-frozen for RNAseq, and homogenized for CFU counts. The GI tract was
642 dissected out, the cecum was weighed, and colon length was measured. Sections of the ileum,
643 cecum, and colon were preserved for histology. Luminal contents from each of these sections
644 were homogenized for CFU counting and snap-frozen for metabolomics/DNA extraction, and
645 mucosal scrapings from each section were snap-frozen for RNAseq and/or RT-qPCR.

646

647 ***CFU Counts***

648 Pre-weighed fecal samples were suspended in 500ml of 25% glycerol solution, homogenized for
649 1 minute in a Mini-BeadBeater-96 (no beads, 2400 RPM), and serially diluted in PBS. Overall
650 bacterial load was quantified by plating on Brain Heart Infusion-Supplemented (BHI-S) agar and

651 incubating aerobically and anaerobically at 37°C for 24 hours. Measurements of overall bacterial
652 load were collected for the pilot cohort, as well as all Colonization Resistance experiments.

653 Although we do not have bacterial biomass measurements for the two non-pilot cohorts of the
654 Western Diet Resilience experiment, the Colonization Resistance experiments were carried out
655 identically to these experiments through Day 14 post-ABX, and data from these timepoints may
656 therefore be interpreted in the same manner. These data, collected from 5 separate cohorts and 48
657 mice, recapitulate the bacterial biomass dynamics of the RC-ABX and WD-ABX treatment
658 groups reported in Figure 1B (Fig. S1B, C). Moreover, they indicate no significant loss of
659 bacterial biomass over the course of the experiment in RC-PBS or WD-PBS controls.

660 To evaluate *St* load, pre-weighed fecal or tissue samples were homogenized in 25% glycerol
661 solution as described above, and quantified by plating on LB agar with 25ug/ml nalidixic acid
662 and incubating at room temperature for 24 hours.

663

664 **DNA Extraction**

665 DNA was extracted using the QIAamp PowerFecal Pro DNA kit (Qiagen). Prior to extraction,
666 samples were subjected to mechanical disruption using a bead beating method. Briefly, samples
667 were suspended in a bead tube (Qiagen) along with lysis buffer and loaded on a bead mill
668 homogenizer (Fisherbrand). Samples were then centrifuged, and supernatant was resuspended in
669 a reagent that effectively removed inhibitors. DNA was then purified routinely using a spin
670 column filter membrane and quantified using Qubit.

671

672 **16S rRNA Sequencing**

673 The V4-V5 region within the 16S rRNA gene was amplified using universal bacterial primers –
674 563F (5'-nnnnnnnn-NNNNNNNNNNNN-AYTGGGYDTAAA- GNG-3') and 926R (5'-
675 nnnnnnnn-NNNNNNNNNNNN-CCGTCAATTYHT- TTRAGT-3'), where 'N' represents the
676 barcodes, 'n' are additional nucleotides added to offset primer sequencing. Approximately
677 ~412bp region amplicons were then purified using a spin column-based method (Qiagen),
678 quantified, and pooled at equimolar concentrations. Illumina sequencing-compatible Unique
679 Dual Index (UDI) adapters were ligated onto the pools using the QIAseq 1-step amplicon library
680 kit (Qiagen). Library QC was performed using Qubit and Tapestation and sequenced on Illumina
681 MiSeq platform to generate 2x250bp reads.

682

683 ***Shotgun Metagenomics***

684 Libraries were prepared using 100 ng of genomic DNA using the QIAseq FX DNA library kit
685 (Qiagen). Briefly, DNA was fragmented enzymatically into smaller fragments and desired insert
686 size was achieved by adjusting fragmentation conditions. Fragmented DNA was end repaired
687 and 'A's' were added to the 3' ends to stage inserts for ligation. During ligation step, Illumina-
688 compatible UDI adapters were added to the inserts and the prepared library was PCR amplified.
689 Amplified libraries were cleaned up, and QC was performed using a tapestation. Libraries were
690 sequenced on an Illumina NextSeq 500 to generate 1x150 reads.

691

692 ***Metagenomic Analysis***

693 Raw metagenomics reads were trimmed using Trimmomatic⁴², and a Minoche quality filter⁴³
694 was applied. Reads from all samples were co-assembled using megahit⁴⁴. We then used the
695 anvi'o v7.1⁴⁵ metagenomic workflow to compute coverage for each gene across metagenomes,

696 and to refine metagenome-assembled-genomes (MAGs). Briefly, the workflow uses (1) Prodigal
697 v2.6.3⁴⁶ to identify open-reading frames (ORFs), (2) '*anvi-run-hmm*' to identify single copy core
698 genes from bacteria (n=71) and ribosomal RNAs (n=12) using HMMER v3.3⁴⁷, (3) '*anvi-run-*
699 *pfams*', '*anvi-run-kegg-kofams*', and '*anvi-run-cazymes*' to annotate ORFs with EBI's PFAM
700 database⁴⁸, the KOfam HMM database of KEGG orthologs (KOs)⁴⁹, and the dbCAN CAZyme
701 HMM database⁵⁰, respectively. We used Bowtie2 v2.3.5.1⁵¹ to recruit metagenomic short-reads
702 to the contigs, and samtools v1.11⁵² to convert SAM files to BAM files. We profiled the
703 resulting BAM files with '*anvi-profile*' and used the program '*anvi-merge*' to combine all single
704 profiles into a merged profile for downstream visualization. We used '*anvi-export-gene-*
705 *coverage-and-detection*' to generate coverage tables for downstream analysis in R. '*deseq2*' was
706 used on the exported count data to identify differentially abundant KOs across time points and
707 treatment groups. To identify CAZyme substrate utilization functions, EC numbers from KEGG
708 annotations were used to map to the dbCAN-sub database⁵⁰. All plots were generated with the R
709 package '*tidyverse*'⁵³ or GraphPad Prism (GraphPad Software).

710

711 ***Metabolite Extraction from Fecal/Cecal Material***

712 Metabolites were extracted with the addition of extraction solvent (80% methanol spiked with
713 internal standards and stored at -80°C, Table S5) to pre-weighed fecal/cecal samples at a ratio of
714 100 mg of material per mL of extraction solvent in beadruptor tubes (Fisherbrand; 15-340-154).
715 Samples were homogenized at 4°C on a Bead Mill 24 Homogenizer (Fisher; 15-340-163), set at
716 1.6 m/s with 6 thirty-second cycles, 5 seconds off per cycle. Samples were then centrifuged at -
717 10°C, 20,000 x g for 15 min and the supernatant was used for subsequent metabolomic analysis.

718 Cecal samples were used in lieu of fecal samples for SCFA analysis as the cecum is the primary
719 site of SCFA production via fermentation in the gut⁵⁴.

720

721 ***Metabolite Analysis using GC-EI-MS and Methoxyamine and TMS Derivatization***

722 Metabolites were analyzed using gas chromatography mass spectrometry (GCMS) with electron
723 impact ionization. To a mass spectrometry autosampler vial (Microliter; 09-1200), 100 µL of
724 metabolite extract was added and dried down completely under a nitrogen stream at 30 L/min
725 (top) and 1 L/min (bottom) at 30°C (Biotage SPE Dry 96 Dual; 3579M). To dried samples, 50
726 µL of freshly prepared 20 mg/mL methoxyamine (Sigma; 226904) in pyridine (Sigma; 270970)
727 was added and incubated in a thermomixer C (Eppendorf) for 90 min at 30°C and 1400 rpm.

728 After samples were cooled to room temperature, 80 µL of derivatizing reagent (BSTFA + 1%
729 TMCS; Sigma; B-023) and 70 µL of ethyl acetate (Sigma; 439169) were added and samples
730 were incubated in a thermomixer at 70°C for 1 hour and 1400 rpm. Samples were cooled to RT
731 and 400 µL of Ethyl Acetate was added to dilute samples. Turbid samples were transferred to
732 microcentrifuge tubes and centrifuged at 4°C, 20,000 x g for 15 min. Supernatants were then
733 added to mass spec vials for GCMS analysis. Samples were analyzed using a GC-MS (Agilent
734 7890A GC system, Agilent 5975C MS detector) operating in electron impact ionization mode,
735 using a HP-5MSUI column (30 m x 0.25 mm, 0.25 µm; Agilent Technologies 19091S-433UI)
736 and 1 µL injection. Oven ramp parameters: 1 min hold at 60°C, 16°C per min up to 300°C with a
737 7 min hold at 300°C. Inlet temperature was 280°C and transfer line was 300°C. Data analysis
738 was performed using MassHunter Quantitative Analysis software (version B.10, Agilent
739 Technologies) and confirmed by comparison to authentic standards. Normalized peak areas were
740 calculated by dividing raw peak areas of targeted analytes by averaged raw peak areas of internal

741 standards. Bile acid assays for cholic acid also included allocholic acid; assays for lithocholic
742 acid also included allolithocholic acid and isolithocholic acid.

743

744 ***Histopathology***

745 Cecal tissue cross-sections were fixed with 4% formalin for 24 hours and were stored in 70%
746 ethanol until paraffin embedding and tissue sectioning. Embedding, sectioning, and H&E
747 staining were performed by the University of Chicago Human Tissue Resource Center. Each
748 tissue section was scored for pathology in a blinded fashion by a pathologist and a trained
749 researcher according to the system outlined by Barthel, *et al.*¹⁶ Briefly, two independent scores
750 for submucosal edema, PMN infiltration, goblet cells, and epithelial integrity were averaged for
751 each tissue sample. The combined histopathological score for each sample was determined as the
752 sum of these averaged scores. It ranges between 0 and 12 arbitrary units and covers the following
753 levels of inflammation: 0 = no signs of inflammation; 1-2 = minimal signs of inflammation; 3-4
754 = slight inflammation; 5-8 = moderate inflammation; 9-13 = profound inflammation.

755

756 ***RT-qPCR***

757 Total messenger RNA isolated from colonic mucosal scrapings was used with Transcriptor First
758 Strand cDNA Synthesis Kit (Roche Diagnostics Corporation) to obtain cDNA. Real-time qPCR
759 was performed using iTaq Universal SYBR Green Supermix with CFX384 Real-Time System
760 (Bio-Rad). Primers and cycling conditions were derived from Devlin et al., 2022⁵⁵ (Table S10).
761 Expression was calculated via $\Delta\Delta Ct$ relative to the housekeeping gene *actb* and the control group
762 RC-PBS-PBS.

763

764 ***Construction of Probabilistic Annotation from ASV Sequences***

765 We mapped as many of the ASV sequences as possible from our amplicon sequencing and
766 analysis pipeline to 16S sequences of full reference genomes that are a part of the AGORA2 set
767 of common gut microorganisms⁵⁶. We searched for identical 16S sequences and iteratively
768 reduced the identity threshold by 1% to 90% until a match was acquired, or accepted that the
769 ASV does not have a matching AGORA2 genome if no match was acquired at the 90%
770 threshold. We mapped 3035 distinct AGORA2 reference genomes to 1654 of the experimentally
771 detected ASVs, and then created 267 ASVsets by grouping ASVs whose reference genomes
772 were all more than 50% identical with each other. The ASVsets were named for the most
773 common genus of each set and appended with an iterative suffix if the genus had already been
774 identified by a previous ASVset (e.g. Lactoccocus.1, then Lactoccous.2, *etc*), which indicates
775 that the ASVsets embody sub-genus phylogenetic resolution. All mapped reference genomes
776 were loaded into KBase⁵⁷, annotated with RAST⁵⁸ (<https://narrative.kbase.us/narrative/178418>),
777 and then the reference genomes were merged into a single probabilistic annotation for each
778 ASVset that contains a pseudo function-based gene representing each distinct RAST-assigned
779 function annotated across all reference genomes mapped to the ASVset. A probability p_{func} for
780 each pseudogene in the probabilistic annotation was created from the count of the associated
781 function across the reference genomes of the ASVset divided by the number of reference
782 genomes in the ASVset. These probabilistic annotations were saved in KBase as genome objects,
783 with a name matching the name of the ASVset from which they were derived (see
784 <https://narrative.kbase.us/narrative/181152>). Each pseudogene was annotated with the
785 corresponding RAST function and the associated probability saved in the evidence score. In the

786 alias list for each pseudogene, we included the full list of gene IDs annotated with the associated
787 RAST function across all the reference genomes comprising the probabilistic annotation.

788

789 ***Reconstruction of ASVset prGEMs Based on Probabilistic Annotations***

790 We applied the MS2 - Build Prokaryotic Metabolic Models with OMEGGA app in KBase¹ to
791 reconstruct a draft metabolic model from the probabilistic annotation for each ASVset. Reactions
792 are mapped through this reconstruction process to the pseudo function-based genes comprising
793 each probabilistic annotation. The draft models were gapfilled in glucose minimal media, to
794 ensure that every model includes all the reactions needed to permit growth without any essential
795 auxotrophy, and were further gapfilled on all of the 63 metabolites, to ensure that the models
796 were capable of consumption, production, and growth in metabolic environment determined from
797 our metabolomics data. The gapfilling ensures that all of the pathways needed to interact with the
798 measured metabolites were available and ensures that models can function in diverse contexts
799 that the microbiome environment presents; however, we are not asserting that all ASVs have all
800 of these gapfilled capabilities. All reactions in these ASVset probabilistic genome-scale models
801 (prGEM) are assigned a probability p_{rxn} based on their pseudogene associations. Reactions with
802 pseudogenes are assigned the highest p_{func} associated with any of the pseudogenes to which the
803 reaction was matched (see the previous section for how pseudogene probabilities are computed),
804 while gapfilled reactions are assigned a probability of 0. The prGEMs were saved in KBase
805 using the same name as their associated ASVset: <https://narrative.kbase.us/narrative/181152>.

806

807 ***Generation of Strain-Metabolite Interaction Probability Profiles (SMIPPs)***

808 To gain insights into the metabolic potential of our ASVsets based on their probabilistic
809 annotations, we applied flux balance analysis (FBA) to compute the probability that each ASVset
810 will interact with each of the 63 metabolites measured in our experimental samples. We
811 simulated three possible interactions for each metabolite: (1) consumption and transformation by
812 forcing a negative exchange flux; (2) production, after conversion from a different input nutrient,
813 by forcing a positive exchange flux; and (3) growth by forcing biomass production in a minimal
814 media with the metabolite as the sole carbon source. The forced conditions described above were
815 achieved through tailored FBA constraints and an FBA objective that minimized the product of
816 each forward or reverse reaction flux and the probability that the reaction should not be part of
817 the model: $1 - p_{rxn,i}$ for reaction i . This objective function determines the most likely reactions
818 and pathway for each phenotype, which enables computing an overall probability for each
819 phenotype by averaging the $p_{rxn,i}$ values associated with all the reactions involved in the
820 pathway. Based on this analysis, we created three species-metabolite interaction probability
821 profiles (SMIPPs) across our ASVsets: consumption, production, and growth. These SMIPPs
822 take the form of matrices – $P_{SMIPP,up}$, $P_{SMIPP,ex}$, and $P_{SMIPP,gr}$ for production, consumption, and
823 growth, respectively – where the rows correspond to ASVsets, the columns correspond to
824 metabolites, and the data elements contain the average probability of the reactions used in the
825 associated ASVset prGEM to implement a given phenotype (consumption, production, or
826 growth) with the associated metabolite. We used cluster heatmaps to render the $P_{SMIPP,up}$,
827 $P_{SMIPP,ex}$, and $P_{SMIPP,gr}$ matrices, grouping metabolites and ASVsets that had similar profiles in
828 Figure S5.

829

830 ***Generation of Microbiome-Metabolite Interaction Probability Profiles (MMIPPs)***

831 Combining SMIPPs with microbiome composition data allowed us to translate strain interactions
832 of each SMIPP matrix into sample-wide aggregate microbiome interactions with the same
833 metabolites. The sample ASV abundance matrix, A_{ASV} , was first translated into an ASVset
834 abundance matrix, A_{set} , to align with the SMIPPs that were only available for ASVsets. A_{ASV} has
835 dimensions of a_{strain} (number of ASVs) by s (number of samples), with each element being the
836 ASVset abundance in given a sample. Each ASVset abundance of A_{set} is computed by summing
837 the rows of A_{ASV} for all members of the ASVset. The dot product of A_{set} and each PSMIPP
838 matrix ($P_{SMIPP,up}$, $P_{SMIPP,ex}$, and $P_{SMIPP,gr}$) were computed to produce new corresponding
839 $P_{MMIPP,up}$, $P_{MMIPP,ex}$, and $P_{MMIPP,gr}$ matrices, which are s (# samples) x m (# metabolomics
840 metabolites) matrices with the probabilities that the microbiome in each sample has the
841 metabolic potential to consume, produce, or grow on each measured metabolite.

842

843 ***Correlating Metabolite Interaction Potential with Metabolite Abundance***

844 The P_{SMIPP} matrices importantly represent the metabolic capacity for an interaction, and not the
845 probability of that interaction. Correlating P_{SMIPP} with the metabolite abundance matrix M , an s
846 x m matrix with elements of abundance of each metabolite in each sample, therefore identifies
847 which metabolites might be most impacted by microbial metabolism. Metabolite correlations in
848 Supplementary Table S8 were determined by correlating the probabilities of $P_{SMIPP,up}$, $P_{SMIPP,ex}$,
849 and $P_{SMIPP,gr}$ with the abundances in M . Highly positively or negatively correlated metabolites
850 signify those that are most likely affected by microbial metabolism.

851

852 ***Construction of Community Metabolic Models for Sample Intervals***

853 We created a community prGEM of each interval between experimental samples for which
854 metabolomics data was collected using the compartmentalized community model formalism
855 described in Henry *et al.*, 2016⁵⁹. The $A_{int, set}$ matrix of ASVset abundances per sample interval
856 is derived from the average of A_{set} between adjacent columns (i.e. consecutive timepoints) that
857 defined the interval bounds. Interval community models were built for each column in $A_{int, set}$ by
858 merging the ASVset prGEMs with relative abundances > 1% into a single probabilistic
859 community model (prcGEM). Each ASVset prGEM compartment was assigned an index, which
860 was appended to the IDs of the transport reactions and the intracellular metabolites and reaction
861 IDs of the contained prGEM, while exchange fluxes and extracellular metabolite IDs were
862 shared by all prGEM and thus were not indexed. Finally, the objective function for each prcGEM
863 was defined as one gram of community biomass being the dot product of the biomass flux and
864 ASVset abundance from the $A_{int, set}$ among all merged prGEMs in the interval. The prcGEM
865 therefore contains the union of ASVsets between the samples that define the interval, which
866 allows the model to capture potential ASVsets interactions between the first and second samples
867 of the interval. All of these interval prcGEMs were saved in KBase:
868 <https://narrative.kbase.us/narrative/181152>.

869

870 ***Simulation of Interval Community Models to Predict Maximum Likelihood Interactions***

871 ***Between ASVsets and Metabolites***

872 FBA simulations of each interval prcGEM predicted the maximum-likelihood interactions
873 between the ASVsets and the measured metabolites in each sample interval. Constraints were
874 adjusted to simulate rich media that includes all compounds that can be utilized by any ASVset
875 in the prcGEM, which reflects both uncertainty in and the complexity of the nutritional

876 environment of the gut microbiome. An upper limit of 300 [$\frac{C_{atoms}}{gm_{CDW} \cdot hr}$] was placed on the total
877 carbon uptake of the prcGEM to reflect nutrient limitations, thereby forcing resource competition
878 and incentivizing the consumption of the most nutritious resources. All dipeptide exchanges
879 were forced to zero because they add little value for understanding microbiome behavior yet
880 combinatorially increase complexity compared to simple amino acid exchanges. A flux capacity
881 constraint was added to that limited net flux through each ASVset compartment to less than 750
882 times the growth rate of the compartment, which permits non-auxotrophic optimal growth on
883 glucose in *E. coli* but prevents an ASV from carrying far more flux than is justified by its level of
884 abundance within the microbiome. Oxygen uptake was set to 20 [$\frac{mmol}{gm_{CDW} \cdot hr}$], which means that
885 the microbiome is operating at one-sixth of the oxygen required for fully aerobic growth
886 combined with the specified carbon uptake limit of 300. The community biomass reaction, with
887 all of the aforementioned constraints, was then maximized and constrained to be at least 50% of
888 this optimal growth to force effective community growth while permitting other specifications of
889 the probabilistic optimization to be met. Constraints on the exchange fluxes for metabolites
890 observed in our metabolomics data were then added, such that the exchange flux of metabolites
891 with increasing or decreasing concentration over an interval were forced to be positive or
892 negative, respectively, thereby simulating production or consumption of the metabolite by the
893 microbiome. The fluxes of these concentration-based constraints were increased until just before
894 the optimization became infeasible to optimally replicate the observed metabolite trajectories in
895 the community simulations. Finally, the model objective was defined to minimize the dot
896 product of each reaction flux and the inverse probability ($1 - P_{rxn}$) of the associated prGEM for
897 all ASVset prGEMs to acquire the maximum-likelihood fluxes considering the metabolic

898 capacity and abundance of each individual ASVset for community growth and to reproduce the
899 observed metabolite trajectories.

900 The resultant community fluxes from simulating these communities were visualized in
901 the Escher Map in Figure 3 that depicts metabolic interactions among the ASVsets through the
902 studied ecological successions after antibiotics treatment.

903

904 ***Code availability***

905 The Jupyter Notebooks in which the modeling data was processed and the figures were
906 developed is accessible at https://github.com/HenryLabResearch/ABX_mouse_gut

907

908 ***Data availability***

909 The data, including all DNA sequencing datasets, that support the findings of this study are
910 available in this article, the Supplemental Information, and BioProject accession PRJNA992061.

911

912 **METHODS REFERENCES**

913 38. Howe, A. *et al.* Divergent responses of viral and bacterial communities in the gut microbiome to
914 dietary disturbances in mice. *ISME J* **10**, 1217–1227 (2016).

915 39. Carmody, R. N. *et al.* Diet dominates host genotype in shaping the murine gut microbiota. *Cell Host
916 and Microbe* **17**, 72–84 (2015).

917 40. Turnbaugh, P. J., Bäckhed, F., Fulton, L. & Gordon, J. I. Diet-Induced Obesity Is Linked to Marked
918 but Reversible Alterations in the Mouse Distal Gut Microbiome. *Cell Host and Microbe* **3**, 213–223
919 (2008).

920 41. Diaz-Ochoa, V. E. *et al.* *Salmonella* mitigates oxidative stress and thrives in the inflamed gut by
921 evading calprotectin-mediated manganese sequestration. *Cell Host Microbe* **19**, 814–825 (2016).

- 922 42. Bolger, A. M., Lohse, M. & Usadel, B. Trimmomatic: a flexible trimmer for Illumina sequence data.
923 *Bioinformatics* **30**, 2114–2120 (2014).
- 924 43. Eren, A. M., Vineis, J. H., Morrison, H. G. & Sogin, M. L. A Filtering Method to Generate High
925 Quality Short Reads Using Illumina Paired-End Technology. *PLOS ONE* **8**, e66643 (2013).
- 926 44. Li, D., Liu, C.-M., Luo, R., Sadakane, K. & Lam, T.-W. MEGAHIT: an ultra-fast single-node
927 solution for large and complex metagenomics assembly via succinct de Bruijn graph. *Bioinformatics*
928 **31**, 1674–1676 (2015).
- 929 45. Eren, A. M. *et al.* Anvi'o: an advanced analysis and visualization platform for 'omics data. *PeerJ* **3**,
930 e1319 (2015).
- 931 46. Hyatt, D. *et al.* Prodigal: Prokaryotic gene recognition and translation initiation site identification.
932 *BMC Bioinformatics* **11**, 1–11 (2010).
- 933 47. Eddy, S. R. Accelerated Profile HMM Searches. *PLOS Computational Biology* **7**, e1002195 (2011).
- 934 48. Bateman, A. *et al.* The Pfam protein families database. *Nucleic Acids Research* **32**, D138–D141
935 (2004).
- 936 49. Kanehisa, M. & Goto, S. KEGG: Kyoto Encyclopedia of Genes and Genomes. *Nucleic Acids*
937 *Research* **28**, 27 (2000).
- 938 50. Zhang, H. *et al.* dbCAN2: a meta server for automated carbohydrate-active enzyme annotation.
939 *Nucleic Acids Res* **46**, W95–W101 (2018).
- 940 51. Langmead, B. & Salzberg, S. L. Fast gapped-read alignment with Bowtie 2. *Nature Methods* **2012**
941 9:4 **9**, 357–359 (2012).
- 942 52. Li, H. *et al.* The Sequence Alignment/Map format and SAMtools. *Bioinformatics (Oxford, England)*
943 **25**, 2078–2079 (2009).
- 944 53. Wickham, H. *et al.* Welcome to the Tidyverse. *Journal of Open Source Software* **4**, 1686 (2019).
- 945 54. Morrison, D. J. & Preston, T. Formation of short chain fatty acids by the gut microbiota and their
946 impact on human metabolism. *Gut Microbes* **7**, 189–200 (2016).

- 947 55. Devlin, J. R. *et al.* *Salmonella enterica* serovar Typhimurium chitinases modulate the intestinal
948 glycome and promote small intestinal invasion. *PLOS Pathogens* **18**, e1010167 (2022).
- 949 56. Heinken, A. *et al.* Genome-scale metabolic reconstruction of 7,302 human microorganisms for
950 personalized medicine. *Nat Biotechnol* **41**, 1320–1331 (2023).
- 951 57. Arkin, A. P. *et al.* KBase: The United States Department of Energy Systems Biology
952 Knowledgebase. *Nature Biotechnology* **2018** *36*:7 36, 566–569 (2018).
- 953 58. Aziz, R. K. *et al.* The RAST Server: Rapid Annotations using Subsystems Technology. *BMC*
954 *Genomics* **9**, 75 (2008).
- 955 59. Henry, C. S. *et al.* Microbial Community Metabolic Modeling: A Community Data-Driven Network
956 Reconstruction. *J Cell Physiol* **231**, 2339–2345 (2016).
- 957

958 **ACKNOWLEDGMENTS**

959 We thank the Chang lab members for scientific support received. This work was performed with
960 support from NIH T32DK007074 (M.S.K.), NIH RC2DK122394 (E.B.C.), NIH T32GM007281
961 (M.S.K.), InnoHK via the Hong Kong Innovation and Technology Commission, the Host-
962 Microbe and Tissue and Cell Engineering cores of the UChicago DDRCC, Center for
963 Interdisciplinary Study of Inflammatory Intestinal Disorders (C-IID) - (NIDDK P30 DK042086),
964 the Gastrointestinal Research Foundation of Chicago, and The Simons Foundation (J.B.). C.S.H.,
965 A.F., and K.B. were supported by the KBase project of the U.S. Department of Energy, Office of
966 Science, Office of Biological and Environmental Research (DE-AC02-06CH11357).

967

968 **AUTHOR CONTRIBUTIONS**

969 Conceptualization, M.S.K., E.B.C., J.B.; Methodology, M.S.K., E.B.C., J.B., A.F., K.B., C.S.H.;
970 Formal Analysis, M.S.K., A.F., K.B., C.S.H., A.G.; Investigation, M.S.K., M.C., M.L.S., M.K.,

971 C.C.; Data Curation, M.S.K., K.B., A.F.; Writing – Original Draft, M.S.K; Writing – Review and
972 Editing, M.S.K., A.F., A.G., M.L.S., C.S.H., E.B.C., S.C.N., F.C., D.R., J.B.; Visualization,
973 M.S.K., A.F.; Funding Acquisition, C.S.H., J.B., S.C.N., F.C., E.B.C.

974

975 **COMPETING INTERESTS STATEMENT**

976 The authors declare no competing interests.

977

978 **ADDITIONAL INFORMATION**

979 Supplementary Information is available for this paper.

980 Correspondence and requests for materials should be addressed to E. Chang.

981

982 **EXTENDED DATA FIGURE LEGENDS**

983 **Figure S1: Western diet impairs microbiome taxonomic and biomass recovery from**
984 **antibiotics.** (A) Consumption of ABX- or PBS-spiked water per mouse per day did not differ
985 significantly across any treatment groups (n=4-6/group, one-way ANOVA). (B-C) Microbial
986 CFUs plated on anaerobic BHIS media from all (B) female (n=10-24/group) and (C) male
987 cohorts (n=6/group) through Day 14 of recovery post-ABX. Three of six female cohorts and the
988 male cohort did not undergo 16S analysis as in the rest of Figure 1; these data are therefore
989 excluded from Figure 1A and Table S1A, but are analyzed separately in Table S1B. (D-F)
990 Comparison of alpha diversity metrics across cohorts over time. (D) Faith's phylogenetic
991 diversity; (E) Shannon index; (F) ASV richness. Statistics are presented in Table S2. (G) Mean
992 relative abundances of different microbial families for Cohorts 2 and 3. (H) PCoA of 16S-based
993 microbiome taxonomic composition at the genus level using Bray-Curtis dissimilarity for

994 samples from all treatment groups and cohorts through Day 28 of recovery. (I) Mean Bray-Curtis
995 dissimilarity of antibiotic-treated groups from their respective PBS control groups at each
996 timepoint (Table S2).

997

998 **Figure S2: Microbiome metagenomic recovery dynamics differ across dietary treatments.**

999 (A) Metagenomic functional richness in fecal samples from mice on RC-ABX (blue) and WD-
1000 ABX (red) at the KEGG Category (KCat), KEGG Ortholog (KO), and gene call level as a
1001 percentage of functional richness at Day -3 (pre-ABX) (n=3/group, Table S3). (B) Initial (Day -
1002 3) versus final (Day 28) functional redundancy (genes calls per KO) for mice on RC-ABX (blue)
1003 and WD-ABX (red) (Table S3). For mice on RC-ABX (C-E) or WD-ABX (F-H), counts of
1004 significantly differentially abundant KOs (C, F), and Venn diagrams of depleted (D, G) or
1005 enriched (E, H) KOs across timepoints. KEGG Family mapping of significantly depleted KOs in
1006 mice on (I) RC-ABX or (L) WD-ABX. Roman numerals indicate the subset of KOs depicted in
1007 panels (D) and (G). Relative abundances of significantly enriched KOs in mice on RC-ABX at
1008 (J) Day 2 and (K) Day 4 relative to Day -3. Relative abundances of significantly enriched KOs in
1009 mice on WD-ABX at (M) Day 2 and (N) Day 14 relative to Day -3. See Table S4 for statistics.

1010

1011 **Figure S3: Metabolomic evaluations show distinct recovery dynamics across diets. (A)**

1012 Normalized metabolite abundances for mice on RC-ABX at different timepoints are consistent
1013 across mice. Each vertical block represents a different day of recovery. Each column within a
1014 block represents samples from a different mouse. Abundances are normalized to Day -3 (pre-
1015 ABX) for each mouse. (B) PCoA of fecal metabolomics TMS panel data using Bray-Curtis
1016 dissimilarity for samples from RC-ABX and WD-ABX through Day 14 of recovery. (C) PCoA

1017 of cecal metabolomics TMS panel data using Bray-Curtis dissimilarity for samples from RC-
1018 ABX and WD-ABX through Day 28 of recovery. Cecal samples were used due to availability of
1019 material through Day 28. (D – F) Metagenomic gene abundances (left axis, Materials and
1020 Methods) and normalized metabolite abundances (right axis) over time for mice on RC (top,
1021 blue) and WD (bottom, red). (E) α -galactosidase genes, melibiose and raffinose abundance. (F)
1022 Starch metabolism genes, glucose abundance. (G) Arabinan metabolism genes, arabinose
1023 abundance. See Table S6 for statistics.

1024

1025 **Figure S4: Residual antibiotic concentrations were not significantly different across RC-**
1026 **ABX and WD-ABX groups.** Absolute quantification of fecal (A) vancomycin, (B) neomycin,
1027 and (C) cefoperazone from immediately after cessation fo antibiotic treatment through Day 7 of
1028 recovery. See Table S7 for statistics.

1029

1030 **Figure S5: Strain-metabolite Interaction Probability Profiles (SMIPPs) reveal metabolic**
1031 **specialization.** Heatmaps indicating the probability that a given ASV prGEM (rows) has the
1032 capacity to (A) consume or (B) produce the indicated compounds (columns).

1033

1034 **Figure S6: Network metrics of community flux simulations vary across dietary treatment**
1035 **groups.** (A) Total predicted consumption or production flux through each metabolite category in
1036 mice on RC (blue, top) or WD (red, bottom) over the indicated recovery interval. As recovery
1037 proceeds, mice on RC push more flux through carbohydrate metabolism than mice on WD. (B)
1038 Total edges (i.e. metabolic interactions) in the community flux-balance analysis simulation
1039 networks across dietary groups at each time interval, broken down by (C) production or

1040 consumption edges. The microbiome of mice on RC has more edges at all timepoints, indicating
1041 that they have more/broader metabolite interaction (primarily consumption interactions) than in
1042 mice on WD. (D) Histograms depicting the distribution of edges per ASV across diet groups at
1043 each time interval. Mice on WD have few taxa that interact with a large number of metabolites,
1044 whereas in mice on RC, a broader array of taxa interact with an intermediate number of
1045 metabolites.

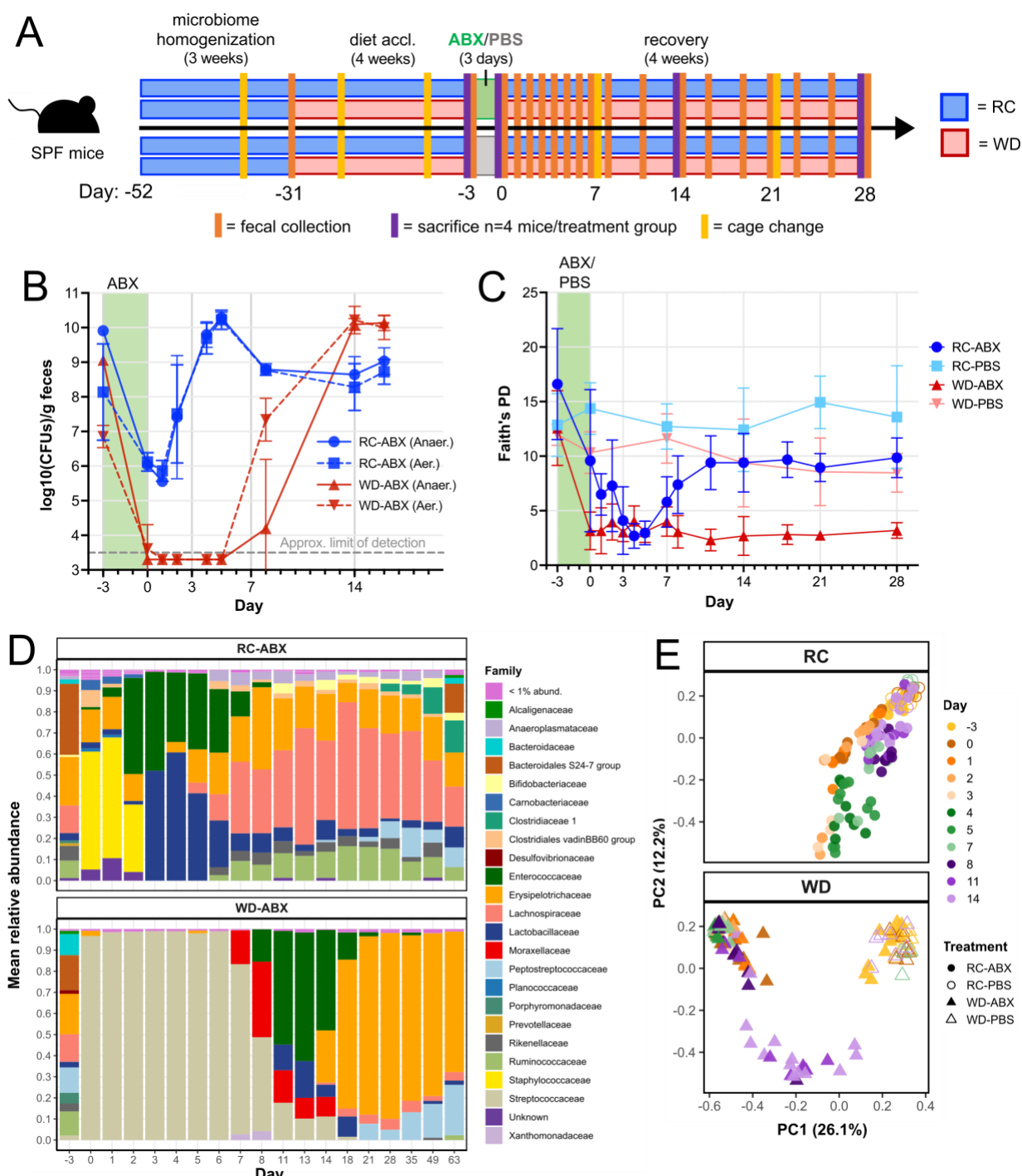
1046

1047 **Figure S7: Dietary intervention and microbial transplant effects through Day 28 of**
1048 **recovery.** PCoA plot of 16S-based taxonomic data for mice on all treatment groups at D14 (A)
1049 and D28 (B) of recovery. Data is paneled according to pre-ABX diet. (C) ASV richness of all
1050 treatment groups through Day 28 of recovery. Data is paneled according to pre-ABX diet. (D)
1051 Mean relative abundances of microbial families at Day 28 across treatment groups.

1052

1053 **Figure S8: Supplemental information regarding colonization resistance experiments.** *St*
1054 CFU counts from female (A) and male (B) cohorts through t=96 hpi. (C) Log10 transformed
1055 Infection AUC for all infected treatment groups. (D) Body weight after infection as a percentage
1056 of pre-infection body weight for all treatment groups. (E) *St* CFU counts across body tissue sites
1057 for all infected treatment groups at t=96 hpi. (F) Cecal and (G) colonic histopathology scoring of
1058 all treatment groups at t=96 hpi broken down by subscore. (H-P) mRNA expression of immune
1059 genes in cecal mucosal scrapings at t=96 hpi based on RT-qPCR. Expression is normalized to the
1060 housekeeping gene Actb and the RC-PBS-PBS treatment group. See Table S10 for statistics and
1061 additional information.

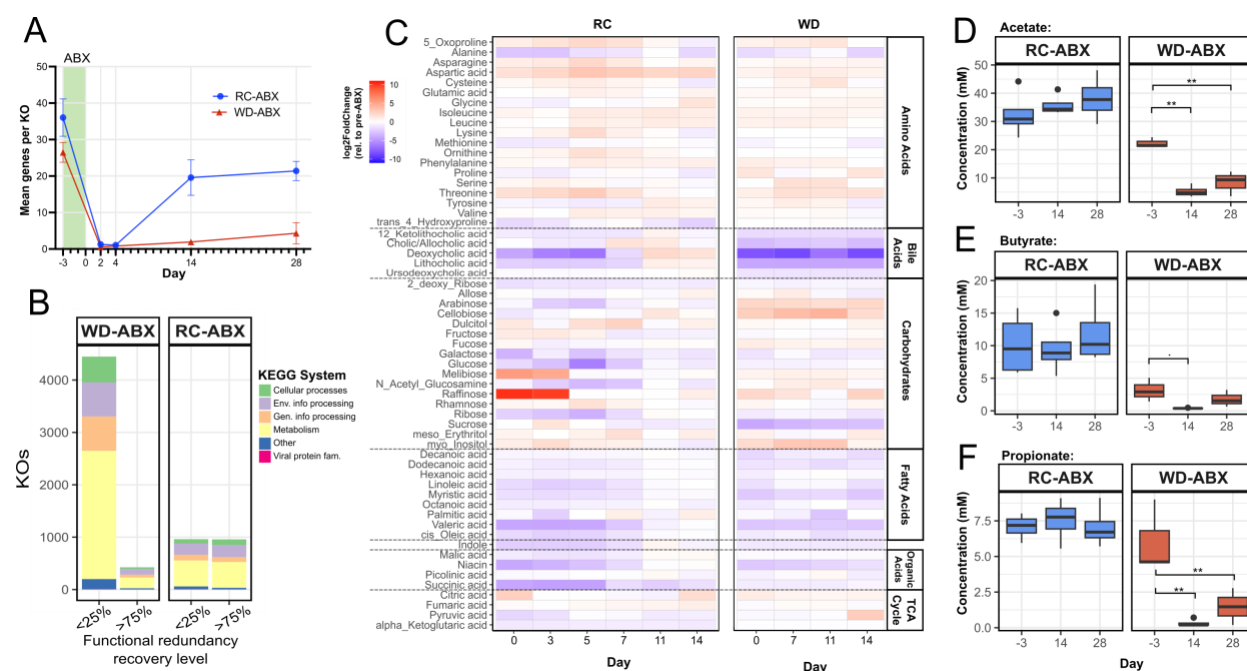
1062 **FIGURES**



1063

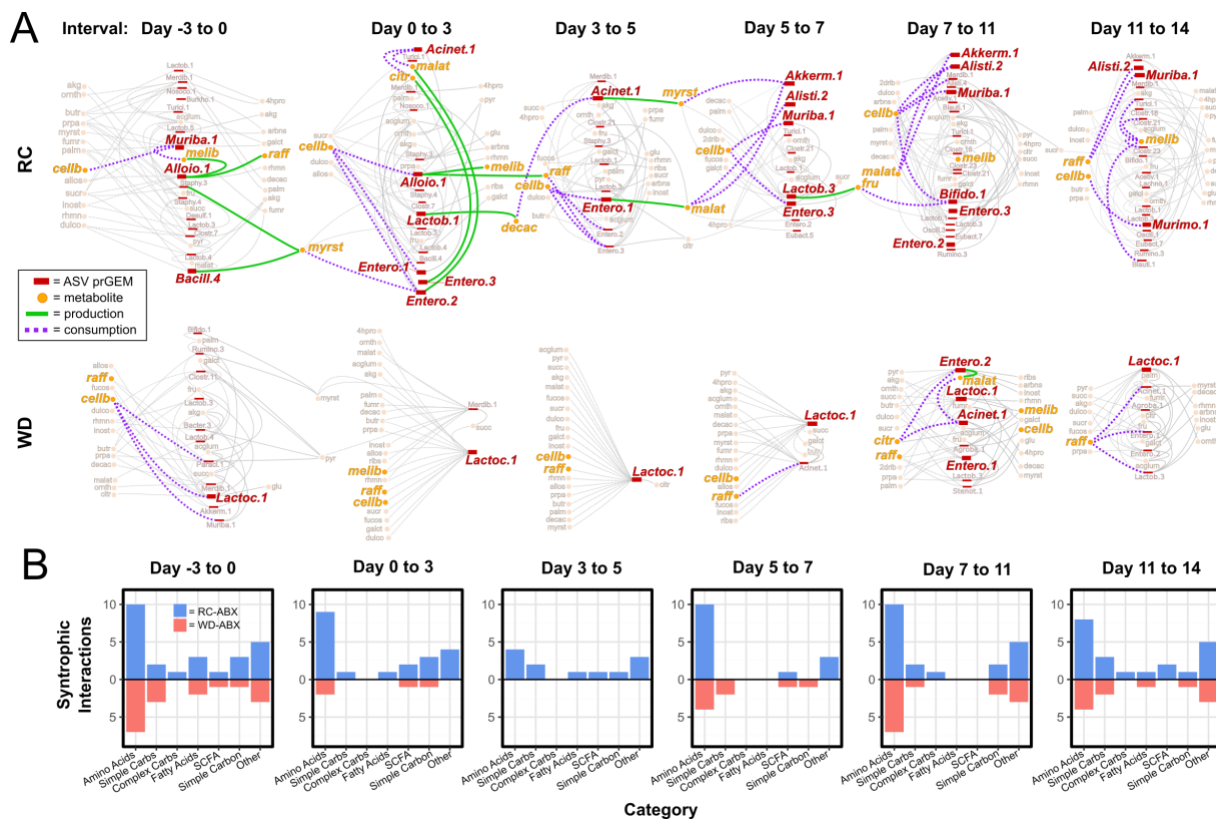
1064 **Figure 1: Bacterial biomass and taxonomic recovery after antibiotic treatment are**
 1065 **impaired in mice on WD. (A) Mice on RC or WD were treated with PBS or ABX in the**
 1066 **drinking water for 72 hours, and serial fecal samples were collected to assess microbiome**

1067 recovery (Materials and Methods). (B) Fecal microbial biomass in mice on RC-ABX and WD-
1068 ABX for mice from Cohort 1 (n=6/group). See also Figure S1A. Error bars indicate mean \pm SD.
1069 Statistics including exact n and P values are presented in Tables S1. (C) Fecal alpha diversity
1070 (phylogenetic diversity) of mice across dietary treatments and timepoints (all cohorts, n=4-
1071 13/group). Error bars indicate mean \pm SD. Statistics including exact n and P values are presented
1072 in Tables S2. (D) Mean relative abundances of different microbial families for Cohort 1 (n=6
1073 mice/group, See Fig. S1F for other cohorts). (E) PCoA of 16S-based microbiome taxonomic
1074 composition at the genus level using Bray-Curtis dissimilarity for samples from all treatment
1075 groups and cohorts through Day 14. See Fig. S1G for results through Day 28.



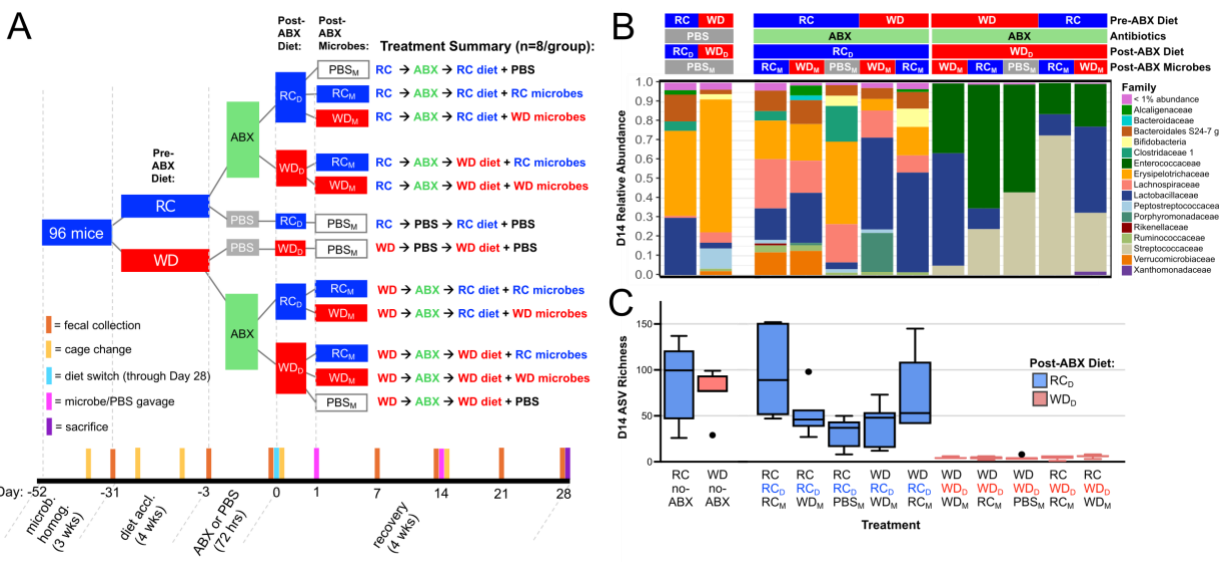
1076

1077 **Figure 2: Functional recovery is severely impaired in mice on WD. (A)** Functional
 1078 redundancy (mean genes per KO) of mice on RC-ABX and WD-ABX (n=2-8/group). Error bars
 1079 indicate mean \pm SD. Statistics including exact n and P statistics are presented in Table S3. (B)
 1080 KEGG system mapping of KOs that recovered < 25% or > 75% of their pre-ABX Day -3
 1081 functional redundancy across RC-ABX and WD-ABX groups. (C) Heatmap displaying
 1082 log2FoldChange in metabolite abundances relative to the pre-ABX Day -3 timepoint, averaged
 1083 across n=3-6 mice/group. (D – F) Absolute concentrations of (D) acetate, (E) butyrate, (F)
 1084 propionate in mice on RC-ABX (blue) and WD-ABX (red) (n=3-4/group, *q < 0.05, **q < 0.01).
 1085 Whiskers represent median \pm 1.5*IQR. Statistics including exact n and P values are presented in
 1086 Table S5.



1087

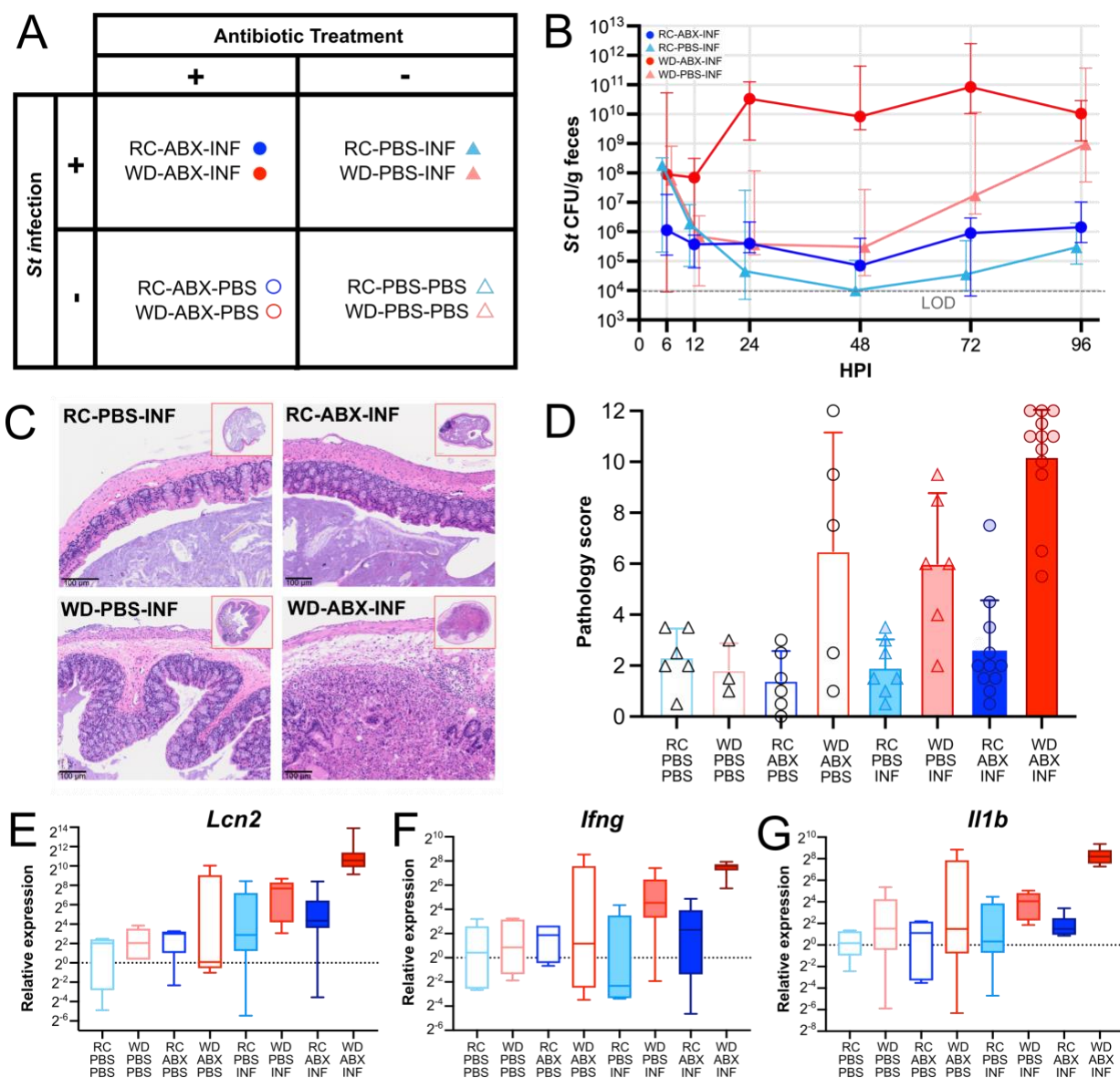
1088 **Figure 3: Metabolic modeling predicts poor syntropy in mice on WD.** (A) Community flux
 1089 simulations over each time interval for mice on RC-ABX or WD-ABX. Edges represent
 1090 predicted flux (dashed = consumption, solid = production) and nodes represent metabolites
 1091 (orange) or ASV prGEMs (red). Select fluxes predicted to play a crucial role in recovery are
 1092 highlighted in green and purple; other fluxes are grey. Map includes all measured metabolites
 1093 with fluxes > 0.05 excluding niacin, acetate, propionate, and amino acids for visual clarity, but
 1094 full model with all flux values is available in Table S8. Interactive map with flux values is
 1095 available at https://modelseed.org/annotation/projects/gut_microbiome/. (B) Number of
 1096 syntrophic interactions identified in the community models for mice on RC (blue) and WD (red)
 1097 by category over each time interval.



1098

1099 **Figure 4: Dietary intervention facilitates microbiome recovery from antibiotics. (A)**

1100 Experimental design. After ABX or PBS, post-ABX dietary treatments (RC_D, WD_D) were
 1101 provided ad libitum from day 0 through the end of the experiment; post-ABX microbial
 1102 treatments (RC_M, WD_M, PBS_M) were administered at Day 1 and Day 14. (B) Mean relative
 1103 abundances of microbial families at Day 14 across treatment groups (n=5-8 mice/group). (C)
 1104 ASV richness across treatment groups at Day 14 (n=5-8/group). Whiskers indicate median ±
 1105 1.5*IQR. Statistics including exact n and P values are presented in Table S9.



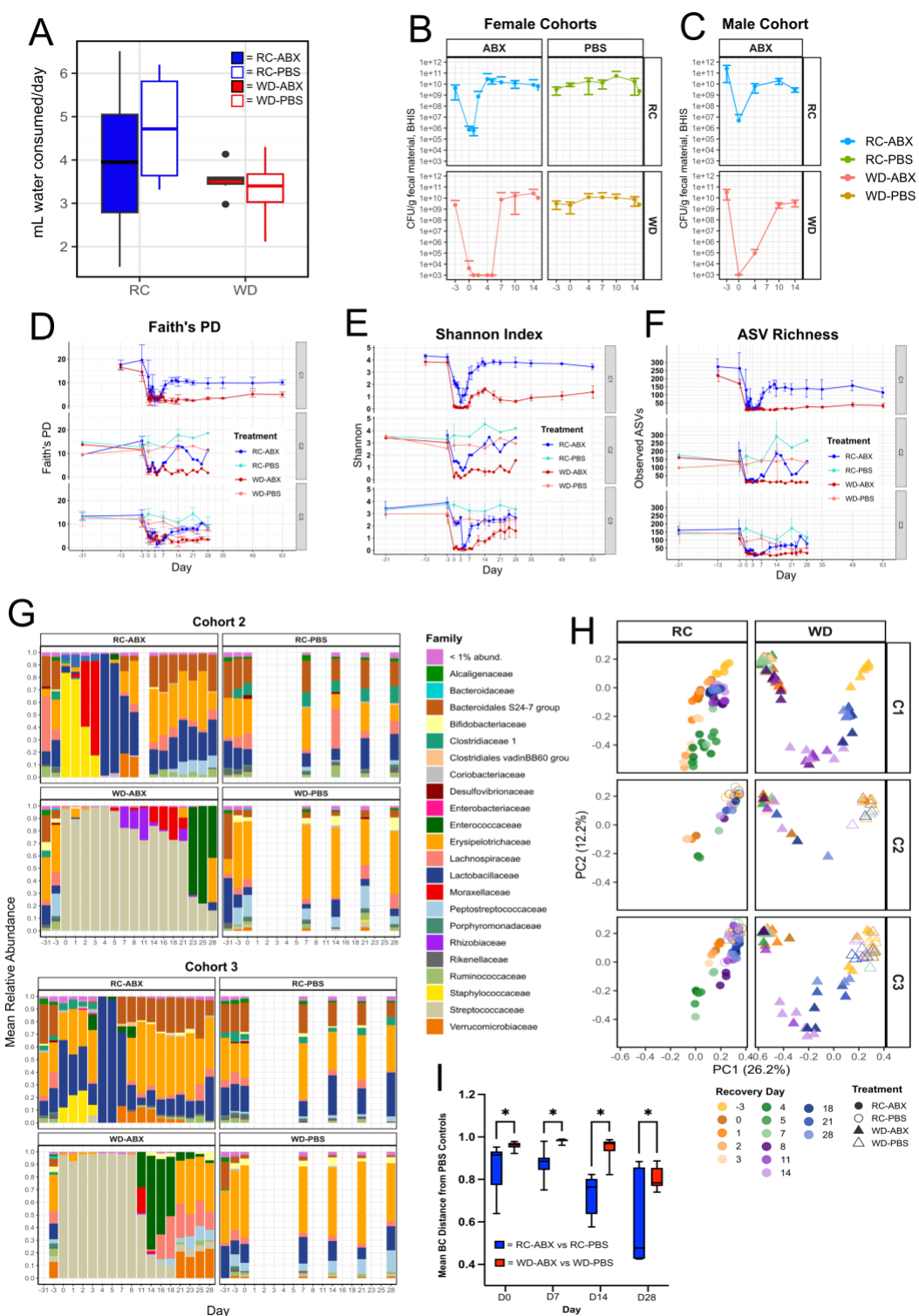
1106

1107 **Figure 5: Prolonged post-antibiotic dysbiosis in mice on WD impairs colonization**

1108 **resistance to St.** (A) Experimental treatment groups. (B) Fecal St load (CFU/g) among infected
 1109 treatment groups. Uninfected controls had no detectable St and are not depicted. Error bars
 1110 indicate median \pm 1.5*IQR. Statistics including exact n and P values are presented in Table S10.
 1111 (C) Representative histological images of mice in different treatment groups. (D)
 1112 Histopathological scoring of cecal sections from mice on indicated treatment groups at 96 hpi
 1113 (n=5–13/group, Figure S8). Error bars indicate mean \pm SD. Statistics including exact n and P

1114 values are presented in Table S10. (E – G) mRNA expression of immune genes in cecal mucosal
1115 scrapings at t=96 hpi based on RT-qPCR (see Figure S8 for additional inflammatory markers).
1116 Expression is normalized to the housekeeping gene Actb and the RC-PBS-PBS treatment group
1117 (n=3-13/group). Whiskers indicate median \pm 1.5*IQR. Statistics including exact *n* and *P* values
1118 are presented in Table S10.

1119 EXTENDED DATA FIGURES

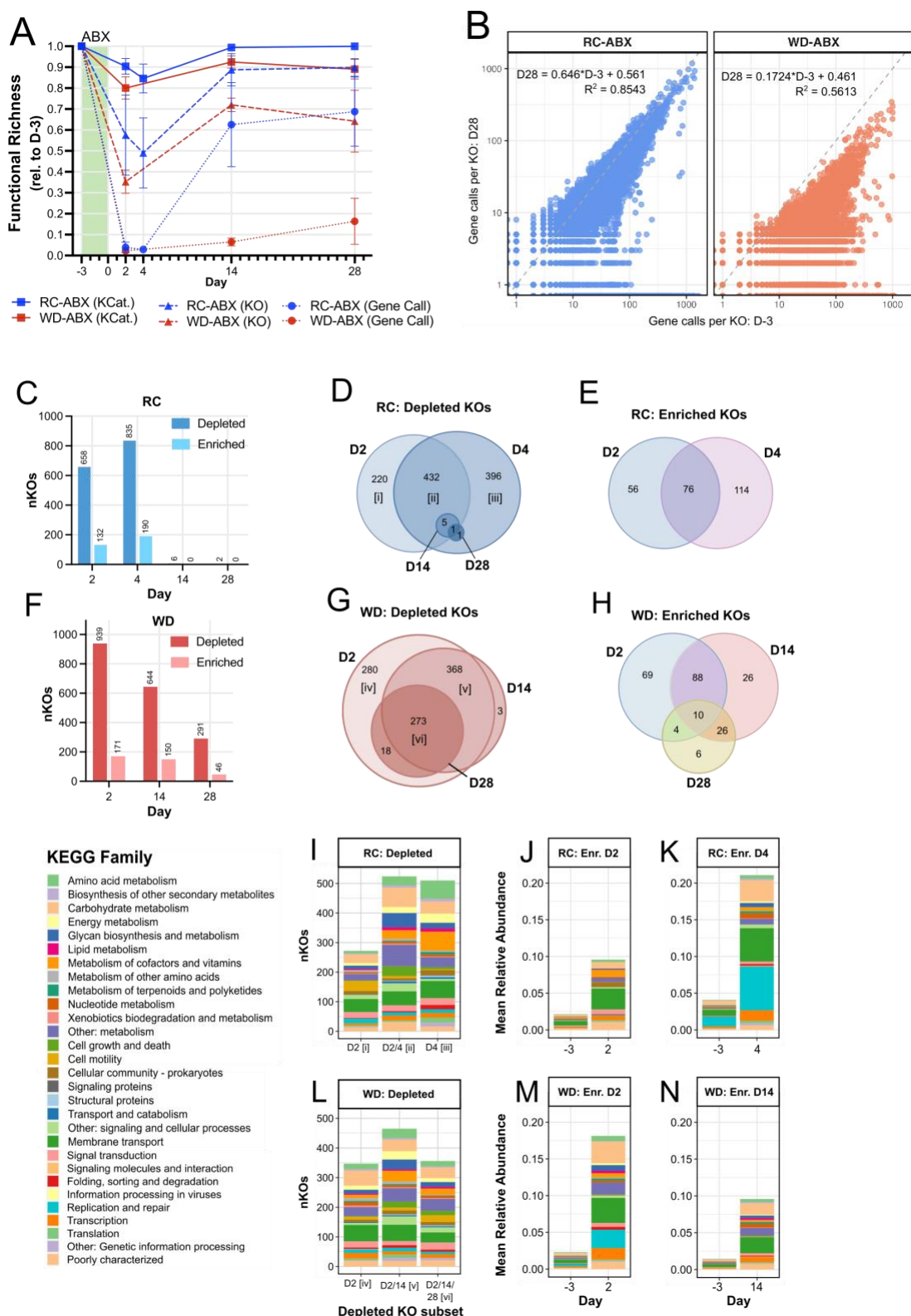


1120

1121 **Figure S1: Western diet impairs microbiome taxonomic and biomass recovery from**
 1122 **antibiotics.** (A) Consumption of ABX- or PBS-spiked water per mouse per day did not differ

1123 significantly across any treatment groups (n=4-6/group, one-way ANOVA). (B-C) Microbial
1124 CFUs plated on anaerobic BHIS media from all (B) female (n=10-24/group) and (C) male
1125 cohorts (n=6/group) through Day 14 of recovery post-ABX. Three of six female cohorts and the
1126 male cohort did not undergo 16S analysis as in the rest of Figure 1; these data are therefore
1127 excluded from Figure 1A and Table S1A, but are analyzed separately in Table S1B. (D-F)
1128 Comparison of alpha diversity metrics across cohorts over time. (D) Faith's phylogenetic
1129 diversity; (E) Shannon index; (F) ASV richness. Statistics are presented in Table S2. (G) Mean
1130 relative abundances of different microbial families for Cohorts 2 and 3. (H) PCoA of 16S-based
1131 microbiome taxonomic composition at the genus level using Bray-Curtis dissimilarity for
1132 samples from all treatment groups and cohorts through Day 28 of recovery. (I) Mean Bray-Curtis
1133 dissimilarity of antibiotic-treated groups from their respective PBS control groups at each
1134 timepoint (Table S2).

1135



1136

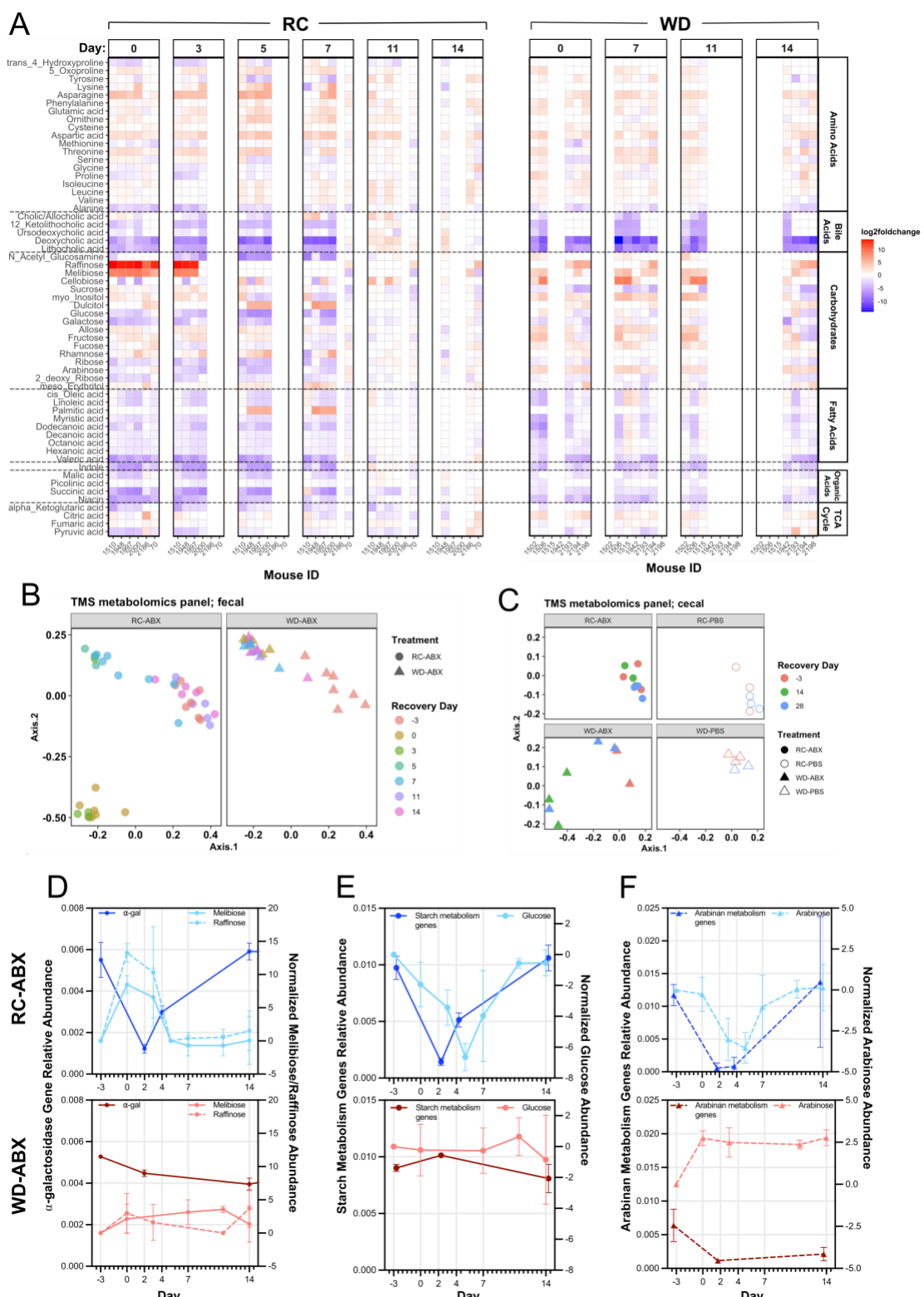
1137 **Figure S2: Microbiome metagenomic recovery dynamics differ across dietary treatments.**

1138 (A) Metagenomic functional richness in fecal samples from mice on RC-ABX and WD-

1139 ABX (red) at the KEGG Category (KCat), KEGG Ortholog (KO), and gene call level as a
1140 percentage of functional richness at Day -3 (pre-ABX) (n=3/group, Table S3). (B) Initial (Day -
1141 3) versus final (Day 28) functional redundancy (genes calls per KO) for mice on RC-ABX (blue)
1142 and WD-ABX (red) (Table S3). For mice on RC-ABX (C-E) or WD-ABX (F-H), counts of
1143 significantly differentially abundant KOs (C, F), and Venn diagrams of depleted (D, G) or
1144 enriched (E, H) KOs across timepoints. KEGG Family mapping of significantly depleted KOs in
1145 mice on (I) RC-ABX or (L) WD-ABX. Roman numerals indicate the subset of KOs depicted in
1146 panels (D) and (G). Relative abundances of significantly enriched KOs in mice on RC-ABX at
1147 (J) Day 2 and (K) Day 4 relative to Day -3. Relative abundances of significantly enriched KOs in
1148 mice on WD-ABX at (M) Day 2 and (N) Day 14 relative to Day -3. See Table S4 for statistics.

1149

1150

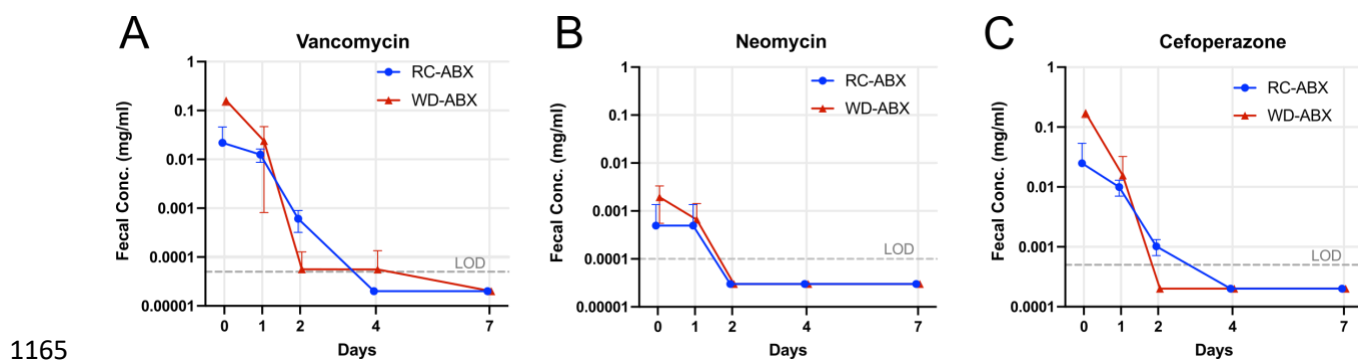


1151

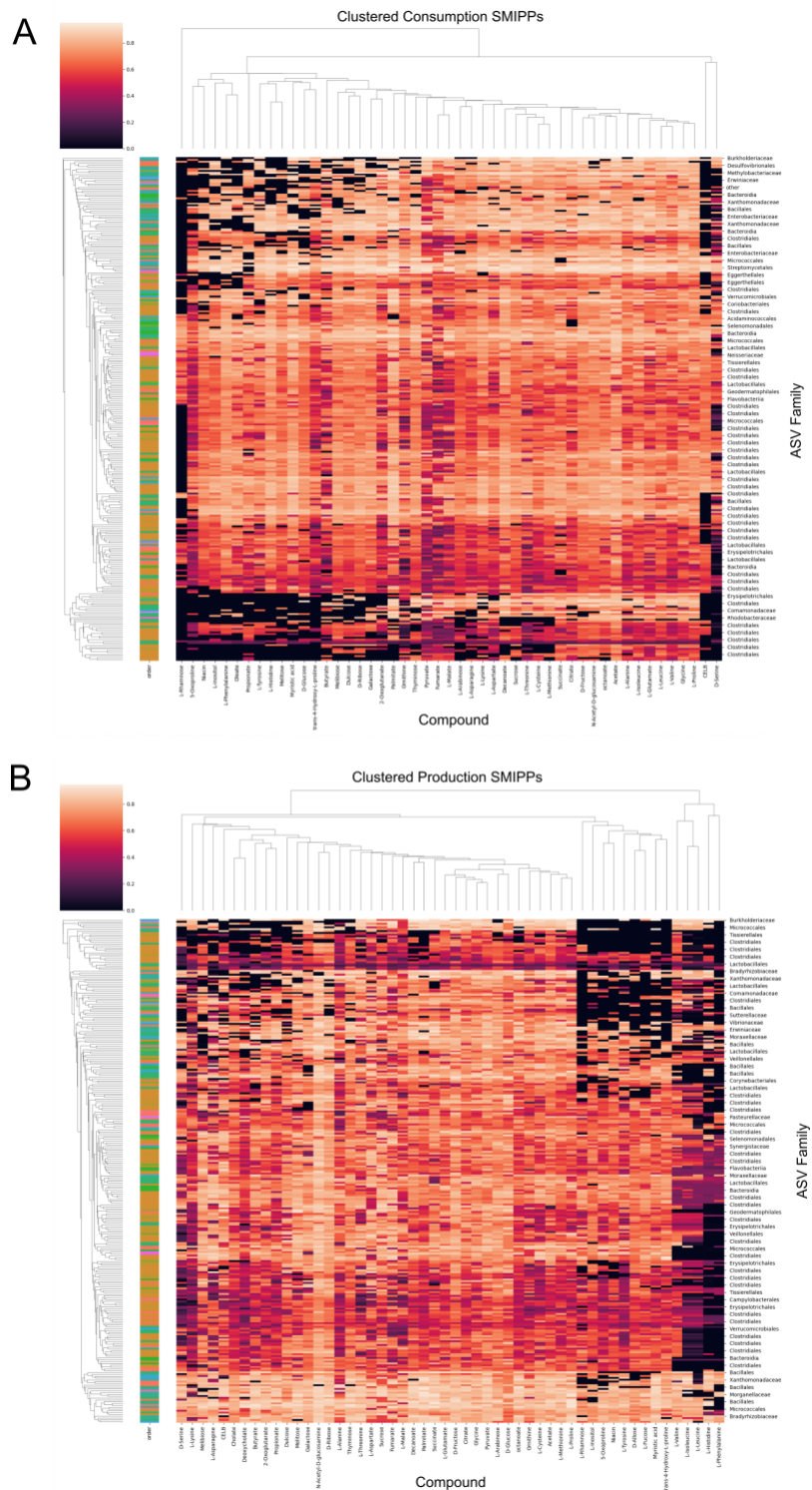
1152 **Figure S3: Metabolomic evaluations show distinct recovery dynamics across diets. (A)**

1153 Normalized metabolite abundances for mice on RC-ABX at different timepoints are consistent

1154 across mice. Each vertical block represents a different day of recovery. Each column within a
1155 block represents samples from a different mouse. Abundances are normalized to Day -3 (pre-
1156 ABX) for each mouse. (B) PCoA of fecal metabolomics TMS panel data using Bray-Curtis
1157 dissimilarity for samples from RC-ABX and WD-ABX through Day 14 of recovery. (C) PCoA
1158 of cecal metabolomics TMS panel data using Bray-Curtis dissimilarity for samples from RC-
1159 ABX and WD-ABX through Day 28 of recovery. Cecal samples were used due to availability of
1160 material through Day 28. (D – F) Metagenomic gene abundances (left axis, Materials and
1161 Methods) and normalized metabolite abundances (right axis) over time for mice on RC (top,
1162 blue) and WD (bottom, red). (E) α -galactosidase genes, melibiose and raffinose abundance. (F)
1163 Starch metabolism genes, glucose abundance. (G) Arabinan metabolism genes, arabinose
1164 abundance. See Table S6 for statistics.



1165
1166 **Figure S4: Residual antibiotic concentrations were not significantly different across RC-**
1167 **ABX and WD-ABX groups.** Absolute quantification of fecal (A) vancomycin, (B) neomycin,
1168 and (C) cefoperazone from immediately after cessation fo antibiotic treatment through Day 7 of
1169 recovery. See Table S7 for statistics.



1170

1171 **Figure S5: Strain-metabolite Interaction Probability Profiles (SMIPPs) reveal metabolic**
1172 **specialization.** Heatmaps indicating the probability that a given ASV prGEM (rows) has the
1173 capacity to (A) consume or (B) produce the indicated compounds (columns).

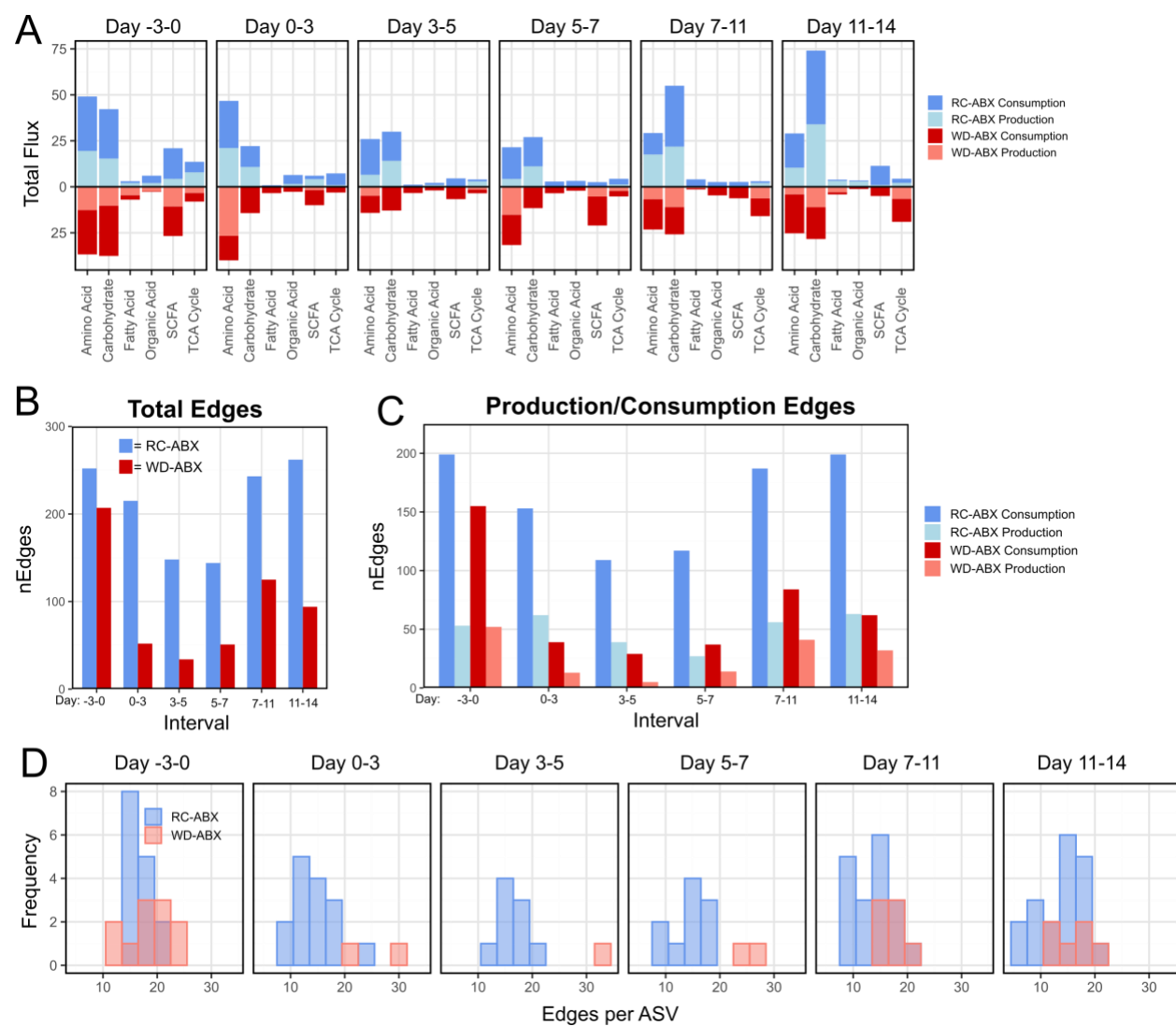
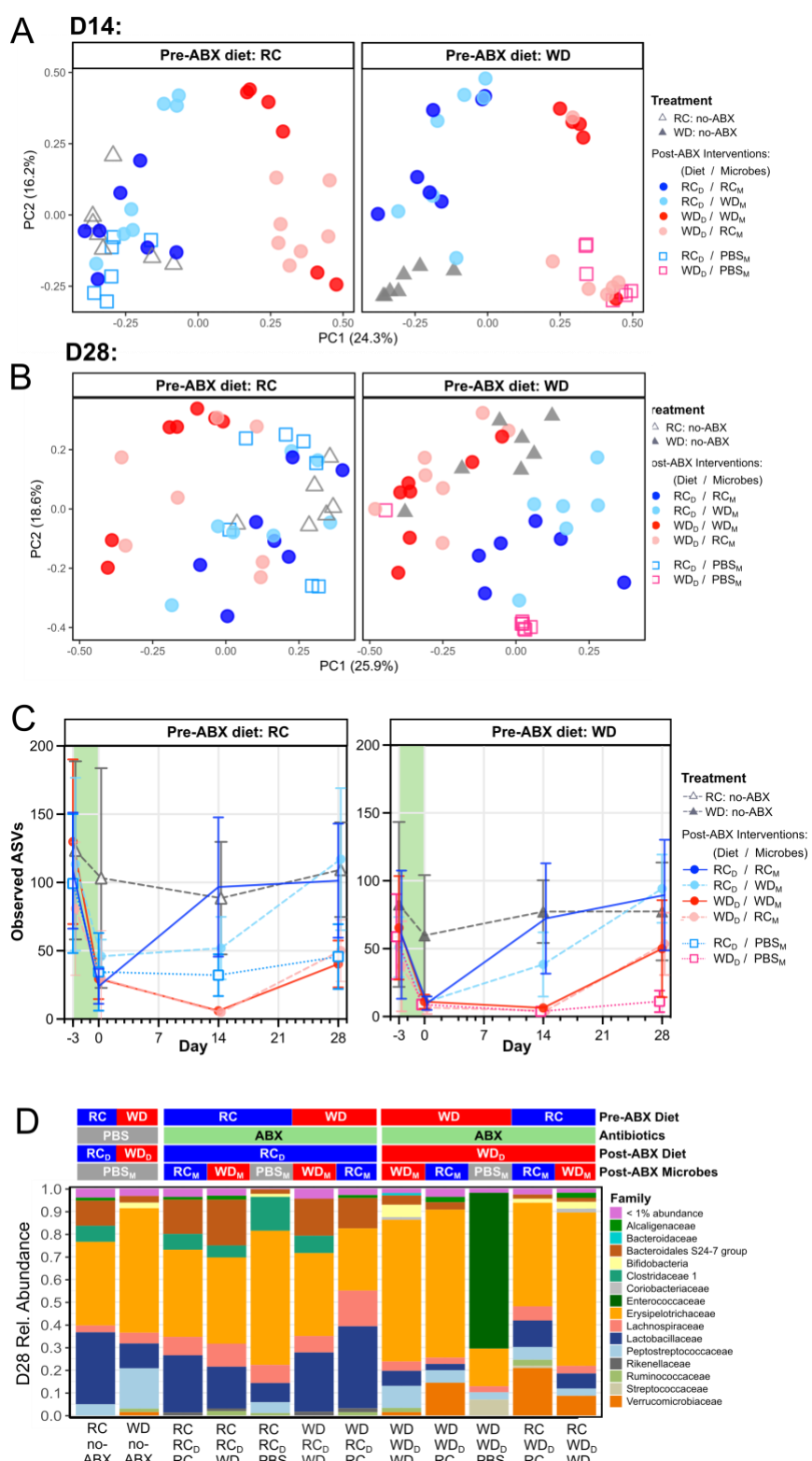


Figure S6: Network metrics of community flux simulations vary across dietary treatment

1176 **groups.** (A) Total predicted consumption or production flux through each metabolite category in
 1177 mice on RC (blue, top) or WD (red, bottom) over the indicated recovery interval. As recovery
 1178 proceeds, mice on RC push more flux through carbohydrate metabolism than mice on WD. (B)
 1179 Total edges (i.e. metabolic interactions) in the community flux-balance analysis simulation
 1180 networks across dietary groups at each time interval, broken down by (C) production or
 1181 consumption edges. The microbiome of mice on RC has more edges at all timepoints, indicating
 1182 that they have more/broader metabolite interaction (primarily consumption interactions) than in

1183 mice on WD. (D) Histograms depicting the distribution of edges per ASV across diet groups at
1184 each time interval. Mice on WD have few taxa that interact with a large number of metabolites,
1185 whereas in mice on RC, a broader array of taxa interact with an intermediate number of
1186 metabolites.

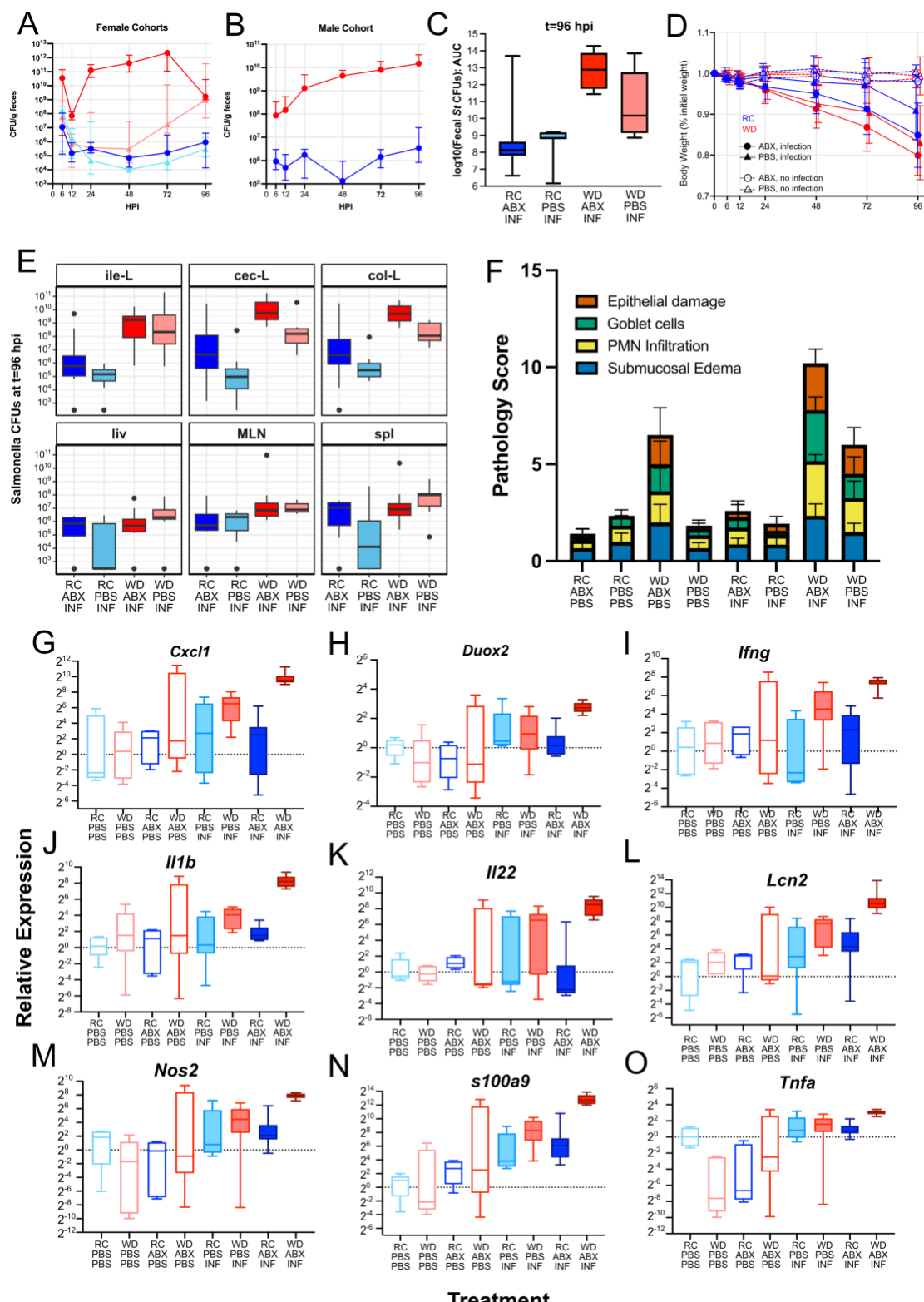


1187

1188 **Figure S7: Dietary intervention and microbial transplant effects through Day 28 of**

1189 **recovery. PCoA plot of 16S-based taxonomic data for mice on all treatment groups at D14 (A)**

1190 and D28 (B) of recovery. Data is paneled according to pre-ABX diet. (C) ASV richness of all
1191 treatment groups through Day 28 of recovery. Data is paneled according to pre-ABX diet. (D)
1192 Mean relative abundances of microbial families at Day 28 across treatment groups.



1193

1194 **Figure S8: Supplemental information regarding colonization resistance experiments. *St***

1195 CFU counts from female (A) and male (B) cohorts through t=96 hpi. (C) Log10 transformed

1196 Infection AUC for all infected treatment groups. (D) Body weight after infection as a percentage
1197 of pre-infection body weight for all treatment groups. (E) *St* CFU counts across body tissue sites
1198 for all infected treatment groups at t=96 hpi. (F) Cecal and (G) colonic histopathology scoring of
1199 all treatment groups at t=96 hpi broken down by subscore. (H-P) mRNA expression of immune
1200 genes in cecal mucosal scrapings at t=96 hpi based on RT-qPCR. Expression is normalized to the
1201 housekeeping gene Actb and the RC-PBS-PBS treatment group. See Table S10 for statistics and
1202 additional information.